HR-COSMOS: Kinematics of star-forming galaxies at z ∼ 0.9

D. Pelliccia, L. Tresse, B. Epinat, O. Ilbert, N. Scoville, P. Amram, B.C. Lemaux, G. Zamorani

A&A 599, A25 (2017)
DOI: 10.1051/0004-6361/201629064

Astronomy & Astrophysics

HR-COSMOS: Kinematics of star-forming galaxies at $z \sim 0.9$⋆

D. Pelliccia[1], L. Tresse[2], B. Epinat[1], O. Ilbert[1], N. Scoville[3], P. Amram[1], B. C. Lemaux[4], and G. Zamorani[5]

[1] Aix Marseille Université, CNRS, LAM (Laboratoire d'Astrophysique de Marseille) UMR 7326, 13388 Marseille, France
e-mail: debora.pelliccia@lam.fr
[2] Univ. Lyon, ENS Lyon, Univ. Lyon 1, CNRS, Centre de Recherche Astrophysique de Lyon UMR5574, 69007 Lyon, France
[3] California Institute of Technology, MC 249-17, 1200 East California Boulevard, Pasadena, CA 91125, USA
[4] University of California Davis, 1 Shields Avenue, Davis, CA 95616, USA
[5] INAF–Osservatorio Astronomico di Bologna, via Ranzani 1, 40127 Bologna, Italy

Received 6 June 2016 / Accepted 19 September 2016

ABSTRACT

We present the kinematic analysis of a sub-sample of 82 galaxies at $0.75 < z < 1.2$ from our new survey HR-COSMOS aimed to obtain the first statistical sample to study the kinematics of star-forming galaxies in the treasury COSMOS field at $0 < z < 1.2$. We observed 766 emission line galaxies using the multi-slit spectrograph ESO-VLT/VIMOS in high-resolution mode ($R = 2500$). To better extract galaxy kinematics, VIMOS spectral slits have been carefully tilted along the major axis orientation of the galaxies, making use of the position angle measurements from the high spatial resolution HST/ACS COSMOS images. We constrained the kinematics of the sub-sample at $0.75 < z < 1.2$ by creating high-resolution semi-analytical models. We established the stellar-mass Tully-Fisher relation at $z \simeq 0.9$ with high-quality stellar mass measurements derived using the latest COSMOS photometric catalog, which includes the latest data releases of UltraVISTA and *Spitzer*. In doubling the sample at these redshifts compared with the literature, we estimated the relation without setting its slope, and found it consistent with previous studies in other deep extragalactic fields assuming no significant evolution of the relation with redshift at $z \lesssim 1$. We computed dynamical masses within the radius $R_{2.2}$ and found a median stellar-to-dynamical mass fraction equal to 0.2 (assuming Chabrier IMF), which implies a contribution of gas and dark matter masses of 80% of the total mass within $R_{2.2}$, in agreement with recent integral field spectroscopy surveys. We find no dependence of the stellar-mass Tully-Fisher relation with environment probing up to group scale masses. This study shows that multi-slit galaxy surveys remain a powerful tool to derive kinematics for large numbers of galaxies at both high and low redshift.

Key words. galaxies: evolution – galaxies: kinematics and dynamics – galaxies: high-redshift – galaxies: statistics – surveys

1. Introduction

In the local Universe, we distinguish a clear bimodality distribution of galaxies in two types with red and blue rest-frame colors, commonly referred to as the red sequence and blue cloud, with a lack of galaxies at intermediate colors (Blanton et al. 2003; Baldry et al. 2004). These color classes are strongly correlated with morphology, so that the blue cloud region is mostly populated by rotating star-forming galaxies (usually spiral) and on the red sequence we find generally quiescent ellipticals, though there is a rare population of red spirals which overlaps the red sequence and may arise from truncated star formation (Masters et al. 2010; Cortese 2012). Star-forming galaxies at high redshift ($z > 0.1$) exhibit a larger diversity of kinematics than in the local Universe ($z \ll 0.1$), and higher fractions of such galaxies are not dominated by rotation or have complex kinematic signatures owing to merging processes (Conselice et al. 2003; Hammer et al. 2009; Kassin et al. 2012; Puech et al. 2012).

Kinematics enables us to trace galaxy properties from high to low redshift and to constrain the galaxy formation scenario using, for example, the well established scaling relation for rotating galaxies observed for the first time by Tully & Fisher (1977) between the optical luminosity and HI line width. The Tully-Fisher (TF) relation is a key to understand the structure and evolution of disc galaxies, since it probes the dark matter halos with their luminous baryonic components, and thus constrains the galaxy formation and evolution models (e.g., Dalcanton et al. 1997; Sommer-Larsen et al. 2003). Later works have shown that the TF relation becomes tighter when defined using microwave to infrared luminosity (Verheijen 1997), and even tighter when luminosity is replaced by the galaxy's stellar mass (Pizagno et al. 2005) or total baryonic mass (McGaugh 2005).

The stellar mass Tully-Fisher (smTF) relation has been studied in the local Universe (Bell & de Jong 2001; Pizagno et al. 2005; Courteau et al. 2007; Reyes et al. 2011) and it appears to be remarkably tight. However, the relation is not yet well defined at higher redshift. Past studies have investigated possible evolution of the smTF relation with conflicting results. Conselice et al. (2005) was the first to look at the smTF relationship at intermediate redshift using the longslit spectroscopy technique with a sample of 101 disc galaxies with near-IR photometry, finding no evidence for an evolution of the relation from $z = 0$ to $z = 1.2$. Puech et al. (2008, 2010) constrained the smTF relation at $z \sim 0.6$ for a small sample of 16 rotating disc galaxies (out of 64 analyzed), part of the IMAGES survey, and they found an evolution of the relation towards lower stellar masses. A slit-based survey with DEIMOS multi-object spectrograph on *Keck* (Faber et al. 2003) was presented by Miller et al. (2011) who have sampled a larger number of galaxies ($N = 129$) at $0.2 < z < 1.3$, showing no statistically significant evolution of the smTF relation, though an evident evolution of the B-band

⋆ Based on observations made with ESO Telescopes at the La Silla Paranal Observatory under programme ID 083.A-0935.

TF with a decrease in luminosity of $\Delta M_B = 0.85 \pm 0.28$ mag from $\langle z \rangle \simeq 1.0$ to 0.3.

Furthermore, it is unclear whether an evolution with redshift of the intrinsic scatter around the TF relation exists. Kannappan et al. (2002) have shown how the scatter around the TF relation in the local Universe increases by broadening their spiral sample, for which the relation is computed, to include all morphologies. Since galaxies at higher redshift show more irregular morphology (Glazebrook et al. 1995; Förster Schreiber et al. 2009), we expect to observe an increase in the scatter with redshift. Puech et al. (2008, 2010) argue that the increase in intrinsic scatter around the TF relation was due to the galaxies with complex kinematics. Kassin et al. (2007), as well, looking at the smTF relationship of 544 galaxies ($0.1 < z < 1.2$) from the DEEP2 redshift survey (Newman et al. 2013a), have found a large scatter (~1.5 dex in velocity) dominated by the more disturbed morphological classes and the lower stellar masses. Conversely Miller et al. (2011) reported a very small intrinsic scatter around the smTF relation throughout their whole sample at $0.2 < z < 1.3$.

The large scatter around the TF relation for broadly selected samples, may also depend on properties external to the galaxies. Environment, for example, is known to have a strong impact on galaxy parameters (Baldry et al. 2006; Bamford et al. 2009; Capak et al. 2007; Sobral et al. 2011; Scoville et al. 2013) and we could expect to see environmental effects also on the TF relation. An alteration in the TF relation in a dense environment, for example, could be due to a temporary increase of the star formation activity or to kinematic asymmetry owing to dynamical interaction of galaxies. Nevertheless, studies on the effects of the environment on the TF relation are still few. Mocz et al. (2012) constrained the TF relation in the u, g, r, i, and z bands and smTF for a local Universe sample of 25 698 late spiral galaxies from the Sloan Digital Sky Survey (SDSS) and investigated any dependence of the relation from the environment defined using the local number density of galaxies as a proxy to their host region. They found no strong or statistically significant changes in the TF relation slope or intercept. At intermediate redshifts, some works constrained the TF relation for cluster and field galaxies, but the results are highly discordant. Ziegler et al. (2003) compared the B-band TF relation for a small sample of 13 galaxies from three clusters at $z = 0.3$, $z = 0.42$ and $z = 0.51$ and 77 field galaxies at $0 < z < 1$ observed with the same set up of the clusters, and they have found no significant differences. The same result of no environmental effect was presented by Nakamura et al. (2006) for a still small sample of 13 cluster galaxies and 20 field galaxies between $z = 0.23$ and $z = 0.58$. Conversely, Bamford et al. (2005) with a larger sample of 80 galaxies at $0 < z < 1$ (22 in clusters and 58 in the field) have found a systematic offset of $\Delta M_B = 0.7 \pm 0.2$ mag in the B-band TF relation for the cluster galaxies with respect to the field sample. Moran et al. (2007), as well, computed the scatter around the Ks-band (proxy of the stellar mass) and V-band TF relations at $0.3 \lesssim z \lesssim 0.65$ for 40 cluster galaxies and 37 field galaxies, showing that cluster galaxies are more scattered than the field ones. More recent work of Jaffé et al. (2011) included in their sample group galaxies, for a total of ~150 galaxies at $0.3 < z < 0.9$, and found no correlation between the scatter around the B-band TF and the environment. Whilst Bösch et al. (2013), for a sample of 55 cluster galaxies at $z \sim 0.17$ and 57 field galaxies at $\langle z \rangle = 0.25$, found a slight shift in the intercept of the B-band TF relation to brighter values for field galaxies and no evolution on intercept of the smTF relation.

We emphasize that defining the environment as two extreme regions in the density distribution of galaxies, i.e., galaxy cluster and general field, is an overly coarse binning of the full dynamical range of the density field at these redshifts. There are, indeed, intermediate environments, like galaxy groups, outskirts of clusters, and filaments which are also important (Fadda et al. 2008; Porter et al. 2008; Tran et al. 2009; Coppin et al. 2012; Darvish et al. 2014, 2015). A larger and more homogeneous study to investigate the environmental effect on the kinematics is still needed.

The recent advent of Integral Field Spectroscopy has provided the opportunity to map the kinematics of intermediate/high redshift galaxies. Various surveys have been obtained so far, by making use of the new generation of Integral Field Unit (IFU), such as the SINS (Förster Schreiber et al. 2009) and MASSIV (Contini et al. 2012) surveys with the near-infrared spectrograph SINFONI (Eisenhauer et al. 2003), KMOS^{3D} (Wisnioski et al. 2015) and KROSS (Stott et al. 2016) surveys with the Multi-Object Spectrograph KMOS (Sharples et al. 2013). Kinematic analysis has been also presented with the first set of observations taken with the Multi Unit Spectroscopic Explorer (MUSE) on VLT (Bacon et al. 2015; Contini et al. 2016) which was able to resolve galaxies in the lower stellar mass range down to $10^8\ M_\odot$. One of the principal limiting factors of the IFU surveys to date has been the necessity to observe one object at a time, because of the IFU small field of view (FOV). This limitation has been improved a lot with the new multi-IFU spectrograph KMOS that operates using 24 IFUs, each one with $2.8'' \times 2.8''$ FOV, and the $1' \times 1'$ wide field mode provided by MUSE. However the FOV of those spectrographs remains much smaller than the one that multi-slit spectrographs can provide, such as VLT-VIMOS, which is made of four identical arms, each one with a FOV of $7' \times 8'$, enabling us to observe ~120 galaxies per exposure.

Our new survey HR-COSMOS aims to obtain the first statistical sample to study the kinematics of star-forming galaxies in the COSMOS field (Scoville et al. 2007) at $0 < z < 1.2$. We seek to obtain a sample that is as representative as possible. Thus we apply no morphological pre-selection other than a cut on the axial ratio $b/a < 0.84$ and the position angle $|\mathrm{PA}| \leq 60°$ for an optimal extraction of the kinematic parameters. We make use of the VIsible Multi-Object Spectrograph at ESO-VLT (VIMOS) in high-resolution (HR) mode, which provides the advantageous facility to perfectly align the spectral slits on our masks along the galaxy major axis measured from the high spatial resolution HST/ACS images. In this paper, we present the kinematic analysis of a sub-sample at $0.75 < z < 1.2$. We constrain the smTF relation at $z \sim 0.9$, using rotation velocities extracted with high-resolution semi-analytical models and stellar masses measured employing the latest COSMOS photometric catalog, which includes UltraVISTA and *Spitzer* latest data releases. We investigate possible dependence of the smTF on the environment defined using the local surface density measurements by Scoville et al. (2013), who make use of the 2D Voronoi tessellation technique. We extend the same analysis to the whole sample to investigate any kinematic evolution with redshift in Pelliccia et al. (in prep.), whilst our data set will be described in Tresse et al. (in prep.).

The paper is organized as follows. In Sect. 2 we present our HR-COSMOS data set, describing the selection criteria, the data reduction process, and the measurements of the stellar masses. In Sect. 3 we describe the method used to create the kinematic models and to fit them with the observed data. The results are presented in Sect. 4, showing the constrained smTF relation at $z \sim 0.9$, the dynamical mass measurements and the

smTF relation as a function of the environment. We summarize our results in Sect. 5.

Throughout this paper, we adopt a Chabrier (2003) initial mass function and a standard ΛCDM cosmology with $H_0 = 70$ km s^{-1} Mpc^{-1}, $\Omega_\Lambda = 0.73$, and $\Omega_M = 0.27$. Magnitudes are given in the AB system.

2. Data

2.1. The HR-COSMOS survey

Our data set at $z \sim 0.9$ is part of an observational campaign (PI: L. Tresse) aimed to measure the kinematics of ~800 emission line galaxies at redshift $0 < z < 1.2$ observed with VIMOS in HR mode (Sect. 2.2). The description of the whole survey will be presented in a following paper.

We selected our targets within the Cosmic Evolution Survey (COSMOS) field (Scoville et al. 2007), a ~2 deg^2 equatorial field imaged with the Advanced Camera for Survey (ACS) of the *Hubble* Space Telescope (HST). This HST/ACS treasury field has been observed by most of the major space-based telescope (*Spitzer*, *Herschel*, *Galex*, *XMM-Newton*, *Chandra*) and by many large ground based telescopes (Subaru, VLA, ESO-VLT, ESO-VISTA, UKIRT, CFHT, *Keck*, and others). Thus we have access to a wide range of physical parameters of the COSMOS galaxies. Emission-line targets have been selected using the spectroscopic information from the zCOSMOS *10k*-bright sample (Lilly et al. 2007) acquired with VIMOS at medium resolution ($R = 580$), and selected with $I_{AB} < 22.5$ and $z < 1.2$. We chose spectra with reliable spectroscopic redshifts (flags = 2,3,4) and emission line flux $f_{line} > 10^{-17}$ erg/s/cm^2 for at least one emission line amongst [OII]λ3727, H$\beta\lambda$4861, [OIII]λ5007, H$\alpha\lambda$6563, lying away from sky lines and visible in VIMOS HR ($R = 2500$) grism spectral range. To fill the VIMOS masks we added a smaller sample of galaxies that have photometric redshift information (Ilbert et al. 2009). For this sample, to increase the probability to target rotating galaxies, we made use of the GINI parameter as morphology measure (Abraham et al. 2003; Lotz et al. 2004; Capak et al. 2007) and selected galaxies with GINI parameter in a range between 0.200 and 0.475.

In Fig. 1 we show the redshift distribution of the whole sample, of which 83% was selected with known spectroscopic redshift. To keep our kinematic sample as representative as possible, we have applied a little pre-selection of the targets:

$z = 0.-1.2$

$I_{AB} \leq 22.5$

$f_{line} > 10^{-17}$ erg/s/cm^2

$-60° \leq PA \leq 60°$

$0 \leq b/a \leq 0.84.$

The first two criteria, the redshift and I_{AB} magnitude, are in common with the zCOSMOS parent sample (Lilly et al. 2007). The condition on the line flux is to ensure the detection of the line visible in VIMOS HR grism spectral range, and the last two selection criteria are chosen for an optimal extraction of the kinematics along the slit. To derive high-quality kinematics, VIMOS spectral slits have been carefully tilted along the major axis orientation of the galaxies. We retained star-forming galaxies with position angle, defined as the angle (East of North) between the North direction in the sky and the galaxy major axis, $|PA| \leq 60°$ since this is the limit to tilt the individual slits of VIMOS from the N-S spatial axis. The condition on axial ratio b/a (ratio between galaxy minor b and major a axis) reflects a condition on the inclination, defined as the angle between the line of sight and the normal to the plane of the galaxy ($i = 0$ for face-on galaxies), and it was applied to analyze the kinematic of galaxies with inclination greater than 30°, since for smaller inclinations the rotation velocity is highly uncertain (small changes in the inclination will result in large changes in the rotation velocity). Both parameters, PA and b/a, have been measured from the high spatial resolution HST/ACS *F814W* COSMOS images by Sargent et al. (2007) using the GIM2D (Galaxy IMage 2D) IRAF software package, which was designed for the quantitative structural analysis of distant galaxies (Simard et al. 2002). These measurements are included in the Zurich Structure and Morphology Catalog[1].

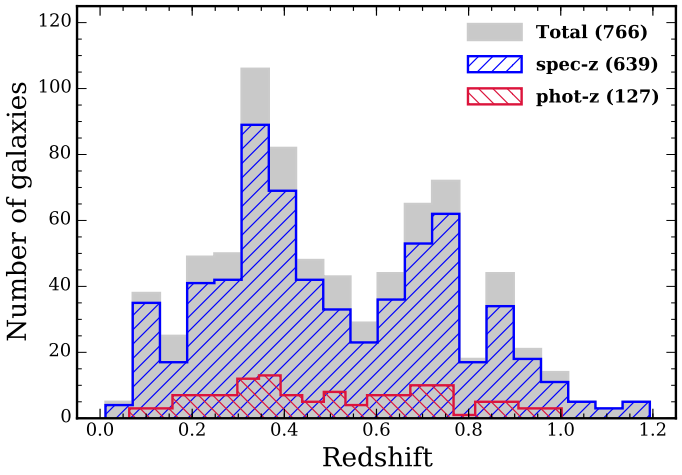

Fig. 1. Redshift distribution of the 766 star-forming galaxies part of our HR-COSMOS survey. The gray filled histogram shows the overall sample and the hashed blue and red histograms represent the sub-samples selected with known spectroscopic redshifts and photometric redshifts, respectively.

In this paper we analyse our data in our highest redshift bin ($0.75 < z < 1.2$), where the doublet [OII]$\lambda\lambda$3726, 3729 is expected.

2.2. Observations

The observations for our kinematic survey were collected over a series of runs between April 2009 and April 2010 with the VIsible Multi-Object Spectrograph (VIMOS, Le Fèvre et al. 2003) mounted on third Unit (Melipal) of the ESO Very Large Telescope (VLT) at the Paranal Observatory in Chile. The targeted area within boundaries of zCOSMOS survey was covered by seven VIMOS pointings, each of them composed of four quadrants, with ~30–35 slits per quadrant. Three exposures were taken for each pointing, for a total exposure time of ~1.5 h per galaxy. Observations details are listed in Table 1.

The 2D spectra have been obtained using the high-resolution grism *HR-red* ($R = 2500$) with the 1″ width slits tilted to follow each galaxy major axis. The manual slit placement was performed using the ESO software VMMPS (VIMOS Mask Preparation Software; Bottini et al. 2005), which enabled us to visually check the correctness of the adopted PA, and in some cases to decide to adjust the slit tilt to get better kinematic

[1] http://irsa.ipac.caltech.edu/data/COSMOS/tables/morphology/

Table 1. Table of observations.

Pointing	α	δ	t_{exp}	Seeing	Date	Period
	J2000	J2000	h:m:s	arcsec		
(1)	(2)	(3)	(4)	(5)	(6)	(7)
P01	10:00:14.400	02:15:00.000	1:40:45	0.796	Dec. 2009, Jan. 2010	P84
P02	10:01:26.400	02:15:00.000	1:40:45	0.893	Mar. 2010	P84
P03	09:59:02.400	02:15:00.000	1:40:45	0.886	Apr. 2009, Dec. 2009	P83, P84
P04	10:01:00.000	02:30:00.000	1:55:20	0.732	Mar. 2010, Apr. 2010	P84, P85
P05	09:59:45.600	02:30:00.000	1:40:45	0.786	Feb. 2010, Mar. 2010	P84
P06	10:01:00.000	02:00:00.000	1:40:45	0.829	Jan. 2010	P84
P07	09:59:45.600	02:00:00.000	1:40:45	0.739	Jan. 2010, Feb. 2010	P84

Notes. Run ID: 083.A-0935(B). (1) Observation pointings; (2) and (3) central coordinates; (4) exposure time; (5) mean seeing over the four quadrants, computed as the FWHM from the spatial profile of the collapsed star spectra present in each quadrant (see text Sect. 2.3); (6) observation dates; (7) ESO Period.

extraction. The wavelength coverage of each observed spectrum is 2400 Å wide, but its range changes according to the position of the slit on the mask. This allowed us to observe emission lines in a wide wavelength range from 5700 Å to 9300 Å. When slits were tilted, the slit width was automatically adjusted to keep constant the width along the dispersion direction, and thus a spectral resolution constant regardless of slit PA. The instrument provides an image scale of 0.205″/pixel and a spectral scale of 0.6 Å/pixel. For the sample analyzed in this paper, at $z \sim 0.9$ the spectral pixel scale is equal, on average, to 25 km s^{-1}. Star spectra have also been obtained, three or four per quadrant, to measure the seeing during each exposure. In total, 766 spectra of emission line galaxies (and ∼90 spectra of stars) have been obtained. In the redshift range ($0.75 < z < 1.2$) analyzed in this paper we have 119 galaxies, of which 17% are part of the targets selected with known photometric redshift and within the specific range of the GINI parameter (see Sect. 2.1). Although we did not target active galactic nucleus (AGN) galaxies, we found two galaxies of our sample as being classified as non-broad-line (NL) AGNs in the catalog of optical and infrared identifications for X-ray sources detected in the XMM-COSMOS survey by Brusa et al. (2010).

2.3. Data reduction

We performed spectroscopic reduction using the VIMOS Interactive Pipeline and Graphical Interface (VIPGI, Scodeggio et al. 2005). The software provides powerful data organizing capabilities, a set of data reduction recipes, and dedicated data browsing and plotting tools to check the results of all critical steps and to plot and analyze final extracted 1D and 2D spectra. The global data reduction process was rather traditional: (1) average bias frame subtraction; (2) location of the spectral traces on the raw frames and computation of the inverse dispersion solution; (3) extraction of rectified 2D spectra and application of the wavelength calibration using the computed inverse dispersion solution; (4) sky subtraction; (5) combination of the three different exposures taken for each target; (6) extraction of 1D spectra. We note that the wavelength calibration task for VIMOS spectra observed in HR mode is somewhat tedious, since the wavelength coverage changes from slit to slit according to where the slit is located on the mask. We have also used the VIMOS ESO pipeline (version 2.9.9), but it does not allow us to combine exposures from different observing nights, therefore we did not proceed further with this tool. Although standard stars have been observed during each observing night, we were not able to perform the spectrum absolute flux calibration. Standard stars spectra were obtained positioning the stars, for each quadrant, at the center of the mask, which did not allow us to produce the calibration for the wide wavelength range of our observations that were obtained thanks to the different positions of the slits on the mask (Sect. 2.2).

The presence of three or four reference star spectra in each quadrant of each pointing allowed the determination of the seeing conditions during spectroscopy acquisitions. This measurement is clearly superior to estimates inferred from the Differential Image Motion Monitor (DIMM; Bösch et al. 2013), since it not only measures this quantity integrated over the entire exposure time of the spectra, but also accounts for systematic effects resulting from observing and co-adding processes. After the reduction (including the combining process of the three different exposures for each target) we collapsed each star spectrum along the spectral direction, and determined the full width at half maximum (FWHM), by fitting a Gaussian function to its spatial profile. We therefore computed seeing conditions in each quadrant as the mean of the FWHMs measured, and we used the determined values in our dynamical analysis. The measured values of the seeing range between 0.57″ and 1.24″, with a median value of 0.8″ during all the observations. The nominal spectral resolution (3 Å, for the grism central wavelength $\lambda_c = 7400$ Å) was checked along the observed spectral range. To that end, we measured the FWHM of four skylines (7275.7 Å, 7750.6 Å, 7841.0 Å, 7913.2 Å) in each slit by fitting a Gaussian function to every single skyline spectral profile. The distribution of the spectral FWHMs ranges between 2.6 Å to 3.2 Å. Since we used the nominal spectral resolution for our models, the measured variation has been taken into account in the error computation of the modeled kinematic parameters (see Sect. 3.3). Although we were provided with the redshift measurement from zCOSMOS, our kinematic analysis requires high precision in measuring the centroid of the emission line, and given the higher resolution of our spectra compared to the ones from zCOSMOS, we re-measured the galaxy redshifts from our 1D reduced spectra.

To facilitate the comparison of the models with the observations we chose to extract ∼40 Å wavelength cutouts around key emission lines of interest (mostly [OII] doublet and a few Hβ in

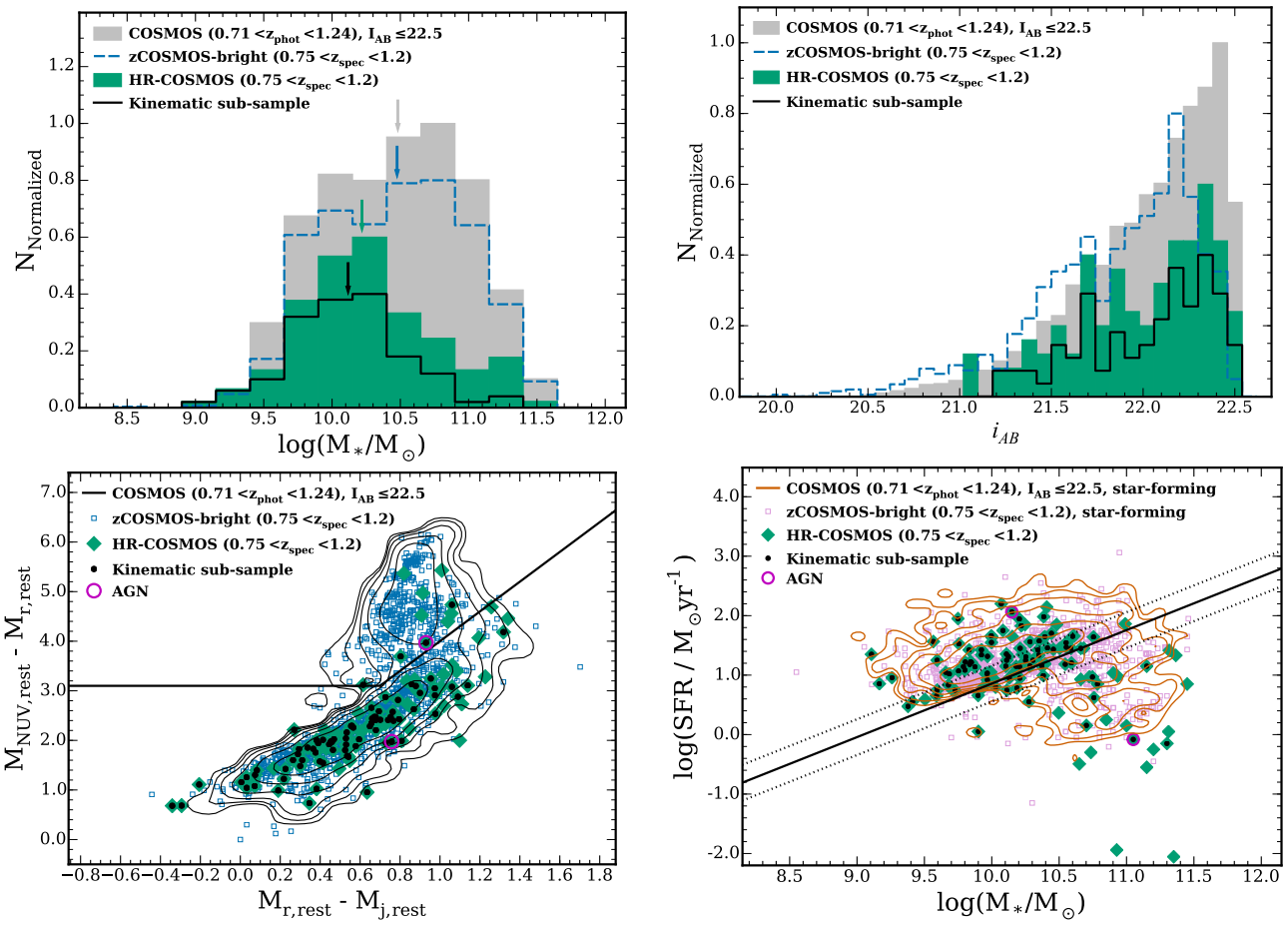

Fig. 2. *Top panels*: stellar mass (*left*) and $I_{\rm AB}$ selection magnitude (*right*) distributions of the 119 galaxies in our sample at $0.75 < z < 1.2$ (green histograms). We show for comparison the distributions of the parent samples in the same redshift range (COSMOS in gray and zCOSMOS-bright in blue) and in black the distribution of 82 galaxies in our kinematic sub-sample (see Sect. 4.1). The photometric redshift range for the COSMOS sample takes into account the precision of the measurements (see text Sect. 2.4). The arrows in *the left panel* show the median of each distribution. The histograms are re-normalized for a better visual comparison of their spreads and peaks, therefore their normalization does not reflect the actual scale. *Bottom left panel*: rest-frame $M_{\rm NUV} - M_{\rm r}$ versus $M_{\rm r} - M_{\rm J}$ color–color diagram. Colors are the same as in the top panels. The contours show the distribution of the COSMOS parent sample with relative number of galaxies equal to 50%, 25%, 13%, 6%, 3%, 1.5% of the maximum of the distribution. The back solid line divides quiescent galaxies (above the line) from star-forming galaxies (below the line) and is determined following the technique adopted by Ilbert et al. (2013). *Bottom right panel*: relationship between SED-derived star formation rate (SFR) and stellar mass. Green diamonds and black points represent the galaxies at $0.75 < z < 1.2$ in our full sample and in our kinematic sub-sample, respectively. The dark-orange contours and the plum open squares show the distribution for the star-forming galaxies (as defined by Laigle et al. 2016) in COSMOS and zCOSMOS-bright samples, respectively. The contours represent the relative number of galaxies at the 50%, 25%, 13%, 6%, 3%, 1.5% of the maximum of the distribution. The solid and dotted lines represent the correlation, with the uncertainties, between the SFR and stellar mass of blue star-forming galaxies at $0.8 < z < 1.2$ by Elbaz et al. (2007). The magenta circles show the AGNs.

our sub-sample at $z \sim 0.75-1.2$) using the HR redshift measurement, and we subtracted the stellar continuum spectrum, since we did not include it in the kinematic models (a cutout with continuum information was also saved for each observation). To perform the continuum subtraction we selected two background regions at the left and right of the emission line (avoiding reduction artifacts and other spectral features), we stacked them, and we computed the median along the wavelength direction, obtaining a spatial profile of the continuum that was subtracted for the entire cutout. During this process we visually inspected all the emission lines of the 119 galaxies in our sub-sample and we decided to discard 28 for which it would have been impossible to retrieve the kinematic information, either because the emission line was too faint, or not detected, or it was shifted at the same wavelength of skylines (even if we selected galaxies with emission lines away from skylines, this could be possible for the targets selected with known photometric redshift for which the measurements uncertainties are larger than for the spectroscopic redshift).

Although the slits were always carefully placed along the major axis of the galaxies (Sect. 2.2), we visually double-checked their correctness and we found that for one galaxy the slit was not well placed. The inclination, adopted for both the sample selection and the kinematic analysis, was also visually inspected by overlapping ellipses with the axial ratio b/a from the Zurich Structure and Morphology Catalog on the HST/ACS *F814W* images of all the galaxies in our sub-sample (see Sect. A). During this visual inspection, we also found that one galaxy was obviously face-on, despite the fact that we selected galaxies with inclination $\gtrsim 30°$ (see Sect. 2.1). Thus, these two galaxies (one with the slit misplaced and one face-one) were not included in our kinematic analysis. This reduced our sample to 89 galaxies, which have been modeled following the method described in Sect. 3.

2.4. Stellar mass measurements

The stellar masses were estimated using the latest COSMOS photometric catalog (Laigle et al. 2016), which makes use of deep *Spitzer* SPASH IRAC imaging (Steinhardt et al. 2014) and the latest release of COSMOS UltraVISTA survey (McCracken et al. 2012). These measurements are extremely accurate since they are based on deep thirty-band UV–IR photometry that covers all galaxy spectral types, and they were obtained using our high-resolution spectroscopic redshift measurements. The measurement technique follows the same recipes presented in Ilbert et al. (2015), based on the Le Phare software (Arnouts et al. 2002; Ilbert et al. 2006). Briefly, the galaxy stellar masses have been derived using a library of synthetic spectra generated with the stellar population synthesis (SPS) package developed by Bruzual & Charlot (2003). We assume a universal IMF from Chabrier (2003), as well as exponentially declining and delayed star formation histories. For all these templates, two metallicities (solar and half-solar) are considered. Emission lines are added following Ilbert et al. (2009), and two attenuation curves are included: the starburst curve of Calzetti et al. (2000) and a curve with a slope 0.9 (Appendix A of Arnouts et al. 2013). The stellar continuum extinction $E_s(B-V)$ is allowed to take values in the range [0–0.7]. The values of the stellar masses were assigned using the median of the stellar mass probability distribution marginalized over all other parameters.

In Fig. 2, we show the distribution of various properties of the HR-COSMOS sample of 119 galaxies in the redshift range $0.75 < z < 1.2$. These are contrasted with the parent zCOSMOS-bright and COSMOS samples. The values for both parent samples are drawn from the latest COSMOS photometric and SED-fitting catalogs (Laigle et al. 2016). For the former parent sample, we compare only those galaxies in the same spectroscopic redshift range as the HR-COSMOS sample presented here. For the latter, the redshift range is extended slightly to $0.75 - 3\sigma_{\Delta z/(1+z_s)} < z < 1.2 + 3\sigma_{\Delta z/(1+z_s)}$ to account for the uncertainties in the photometric redshifts, where $\sigma_{\Delta z/(1+z_s)} = 0.007$.

In the top panels, we present the stellar mass (left) and I_{AB} selection magnitude (right) distributions for our sample of 119 galaxies at $0.75 < z < 1.2$ with green histograms and the distributions of the parent samples in gray (COSMOS) and blue (zCOSMOS-bright). Galaxies in our sample have stellar masses spanning from $1.3 \times 10^9\ M_\odot$ to $2.0 \times 10^{11}\ M_\odot$ and values of I_{AB} spanning from 21.0 mag to 22.5 mag. The black histograms show the distributions of the galaxies used in the kinematic analysis (see Sect. 4). Since we are not interested in comparing the normalization of the distributions, we re-normalized the histograms to better visually compare their spreads and peaks, therefore their normalization does not reflect the actual scale. We measure that the median of the parent samples distributions is equal to $3.0\times10^{10}\ M_\odot$, while the median for the distribution of our samples shifts to lower values ($1.7 \times 10^{10}\ M_\odot$ for the whole sample of 119 galaxies and $1.3\times10^{10}\ M_\odot$ for the kinematic subsample). This may be a result of the fact that our sample is composed primarily of star-forming galaxies and, therefore, the high mass end of the parent samples distributions (probably populated by massive quiescent galaxies) is suppressed in our sample.

In the bottom panels of Fig. 2 we plot the rest-frame $M_{NUV} - M_r$ versus $M_r - M_J$ color–color diagram (left) and the relation between star formation rate (SFR) and stellar mass (right) for our sample compared to the parent samples. The color–color diagram is a diagnostic plot that enables us to separate star-forming from quiescent galaxies. We divide quiescent galaxies from star-forming galaxies following the technique adopted by Ilbert et al. (2013). In the bottom left panel, we show how our sample follows the underling distribution of star-forming galaxies closely. This is supported by the *SFR*-M_* relation displayed in the bottom right panel for the star-forming galaxies (as defined by Laigle et al. 2016) in COSMOS and zCOSMOS-bright samples. The SFR computed from SED fitting is known to be not as precise as that computed using other SFR estimators (Ilbert et al. 2015; Lee et al. 2015). Following Ilbert et al. (2015) we compared the SED-based SFR to the 24 μm IR SFR for the parent COSMOS sample in the redshift range $0.75 < z < 1.2$, and found an offset of 0.15 dex towards larger SED-based SFR. To take into account this discrepancy, we applied a shift of −0.15 dex to the SFR measurements. Our sample follows the star-forming galaxy distribution of the parent samples.

3. Kinematic modeling

To study the galaxy kinematics, we created high-resolution semi-analytic models. The advantage of using a model to constrain the kinematics is that we can compare it directly to the observations, after taking into account all the degradation effects owing to the instrumental resolution, and avoid the intermediate steps of data analysis that can introduce additional noise (Fraternali & Binney 2006).

3.1. The model

Our first step for modeling the galaxy kinematics was to describe an astrophysically-motivated picture of a galaxy at high-resolution. Ionized gas was described as rotating in a thin disc with a certain inclination i and position angle PA of the major axis. A pseudo-observation was created combining high-resolution models of intrinsic flux distribution of the emission line, rotation velocity and dispersion velocity using the following relation:

$$I(r, V) = \frac{\Sigma(r)}{\sqrt{2\pi}\sigma(r)} \exp\left\{-\frac{[V - V(r)]^2}{2\sigma^2(r)}\right\}. \quad (1)$$

This models the galaxy emission at each radius r and reconstructs a 2D emission line to be compared to the observation. If the observed emission was a doublet (as in the case of [OII], the main investigated feature in this study) another contribution was added to the relation, having the same functional form and velocity dispersion σ as the previous one, but shifted in velocity by a fixed value, that was equal to the separation between the two lines of the doublet, and scaled in intensity by a ratio $R_{[OII]}$, an additional parameter of the model. The intrinsic line-flux distribution in the plane of the disc was described by a truncated exponential disc function:

$$\Sigma(r) = \begin{cases} \Sigma_0\, e^{-r/r_0} & \text{if } r < r_{trunc} \\ 0 & \text{if } r > r_{trunc} \end{cases}, \quad (2)$$

where Σ_0 is the line flux at the center of the galaxy, r_0 is the scale radius and r_{trunc} is the maximum radius, after which the emission is no longer detected. The truncation was necessary since we allowed r_0 to assume negative values to better match the observed line flux distribution, in particular when the distribution is characterized by bright clumps in the peripheries of the galaxies.

The velocity along the line of sight, assuming that for spiral galaxies the expansion and the vertical motions are negligible

with respect to the rotation, was described as

$$V(r) = V_{\rm sys} + V_{\rm rot}(r) \sin i \cos\theta, \tag{3}$$

where $V_{\rm sys}$ is the systemic velocity, that is the velocity (corresponding to the systemic redshift) of the entire galaxy with respect to our reference system. For very distant galaxies this quantity is usually dominated by the Hubble flow. Since we are interested only in the galaxy internal kinematics we set it to zero. The galaxy inclination i was measured as the angle between the line of sight and the normal to the plane of the galaxy ($i = 0°$ for face-on galaxy) and θ is the angle in the plane of the galaxy between the galaxy PA and the position where the velocity is measured. Since our model reproduces the emission coming from the slit aligned to the galaxy PA, we assume θ equal zero.

To model the rotation velocity $V_{\rm rot}$, which results from both baryonic (stars and gas) and dark matter potentials, three different functions have been used. All of them are described by two parameters: the maximum velocity $V_{\rm t}$ and the transition radius $r_{\rm t}$. A velocity profile used is the *Freeman disc* (Freeman 1970), which fits a galaxy with a gravitational potential generated by an exponential disc mass distribution. It is expressed as

$$V_{\rm rot}(r) = \frac{r}{h}\sqrt{\pi G \mu_0 h\,(I_0K_0 - I_1K_1)}, \tag{4}$$

where μ_0 is the central surface density and h is the disc scale-length of the surface density distribution. We note that μ_0 and h are not constrained by Σ_0 and r_0 of Eq. (2) since the rotation velocity model does not only describe baryons. I_i and K_i are the i-order modified Bessel function evaluated at $0.5\,r/h$. The maximum velocity

$$V_{\rm t} \sim 0.88\sqrt{\pi G \mu_0 h}, \tag{5}$$

is reached at the transition radius $r_{\rm t} \sim 2.15h$. Substituting Eq. (5) and the transition radius $r_{\rm t}$ in Eq. (4), we obtain an expression of the rotation velocity $V_{\rm rot}$ described by the only two parameters $V_{\rm t}$ and $r_{\rm t}$. Unlike the Freeman disc, the two other rotation curve models are analytic functions that have no physical derivation nor assumed mass distribution, but they appear to describe well the observed rotation curves of local galaxies. The *flat model* consists of a two slopes model, which describes a rotation velocity distribution that has a sharp transition at $r_{\rm t}$ and flats at $V_{\rm t}$. It takes the form:

$$V_{\rm rot}(r) = \begin{cases} V_{\rm t} \times \dfrac{r}{r_{\rm t}} & \text{if } r < r_{\rm t} \\ V_{\rm t} & \text{if } r \geq r_{\rm t}. \end{cases} \tag{6}$$

Last velocity profile adopted is an arctangent function (Courteau 1997), expressed as

$$V_{\rm rot}(r) = V_{\rm t}\frac{2}{\pi}\arctan\frac{2r}{r_{\rm t}}, \tag{7}$$

which smoothly rises and reaches a maximum $V_{\rm t}$ asymptotically at an infinite radius. The transition radius $r_{\rm t}$ is defined as the radius for which the velocity is 70% of $V_{\rm t}$. The galaxy velocity dispersion σ has been modeled to be constant at each radius. This assumption is considered reasonable since it is based on what has been observed in the local Universe in the galaxies from the GHASP sample (Epinat et al. 2008). It has also been shown by some authors (Weiner et al. 2006b; Epinat et al. 2008) that the peak observed in the velocity dispersion profile for galaxies at high redshift is due to the blurring effect of the resolution. The high-resolution model sampling (both spectral and spatial) was chosen to be a sub-multiple of the VIMOS data sampling. We therefore created high-resolution models with spectral and spatial sampling equal to 0.15 Å and 0.05125″, respectively. To make the high-resolution models comparable with the observations, we performed a spatial and spectral smoothing by convolving the models with the spatial resolution given by the seeing measured for each quadrant, and the spectral resolution of the instrument (see Sect. 2.3). The effect due to the slit width was also taken into account by convolving the models with a window function. Finally, the models were re-binned to match the VIMOS sampling (1 pixel = 0.205″ = 0.6 Å).

3.2. The fitting method

The comparison with the observation has been done through the χ^2-minimization fitting using the Python routine MPFIT (Markwardt 2009), based on the Levenber-Marquardt least-squares technique. Preliminary steps were necessary to define a set of initial parameters.

The rotation center, $r_{\rm cen}$ was measured as the center of the continuum spectrum's spatial profile, or, when the continuum emission was too faint, as the center of the emission line's spatial distribution around its observed central wavelength. This last quantity, $\lambda_{\rm line}(z)$, was a parameter of the model that was kept fixed during the fitting process. Using our measured redshift (Sect. 2.3) we derived the systemic velocity $V_{\rm sys}$, which quantifies the motion of the entire galaxy with respect to our reference system. However, for galaxies at high redshift $V_{\rm sys}$ is dominated by the Hubble flow, therefore it is normal practice to set it to zero, to focus only on the internal kinematics. The systemic velocity is allowed to freely vary in the fitting to take into account the effect of the redshift measurement uncertainties. The inclination i is derived from the axial ratio, computed from HST images, found in the literature (Zurich Structure and Morphology Catalog), and corrected for projection effects using Holmberg's oblate spheroid description (Holmberg 1958):

$$i = \arccos\sqrt{\frac{(b/a)^2 - q_0^2}{1 - q_0^2}}, \tag{8}$$

where b/a is the observed axis ratio, $q_0 = c/a$ is the axial ratio of a galaxy viewed edge-on, a and b are the disc major and minor axes, and c is the polar axis. The value of q_0 is known to vary from 0.1 to 0.2 depending on galaxy type (Haynes & Giovanelli 1984). In this study we assumed $q_0 = 0.11$, driven by the necessity to take into account the smallest value of b/a in our sample, that is 0.12, knowing form Pizagno et al. (2005) that the q_0 range 0.1−0.2 corresponds to a small variation (typically $\sim$1 km s^{-1}) in the velocity. Owing to the degeneracy between velocity and inclination (Begeman 1987) we decide to keep i fixed during the fit. The position angle PA is taken from the literature and it is the same used to align the slit along the major axis of the galaxies during the observations (see Sect. 2.2). The PA is fixed in the χ^2 minimization fitting process. Although photometric-kinematic PA misalignment may exist, it has been demonstrated that PA measurements from high-resolution *F814W* images are generally in reasonable agreement with the kinematic PA. Epinat et al. (2009), for a sample of nine galaxies between $1.2 < z < 1.6$ observed with SINFONI, found that the agreement between morphological and kinematic PA is better than 25°, except for galaxies that have a morphology compatible with a galaxy seen face-on. A similar result was found by

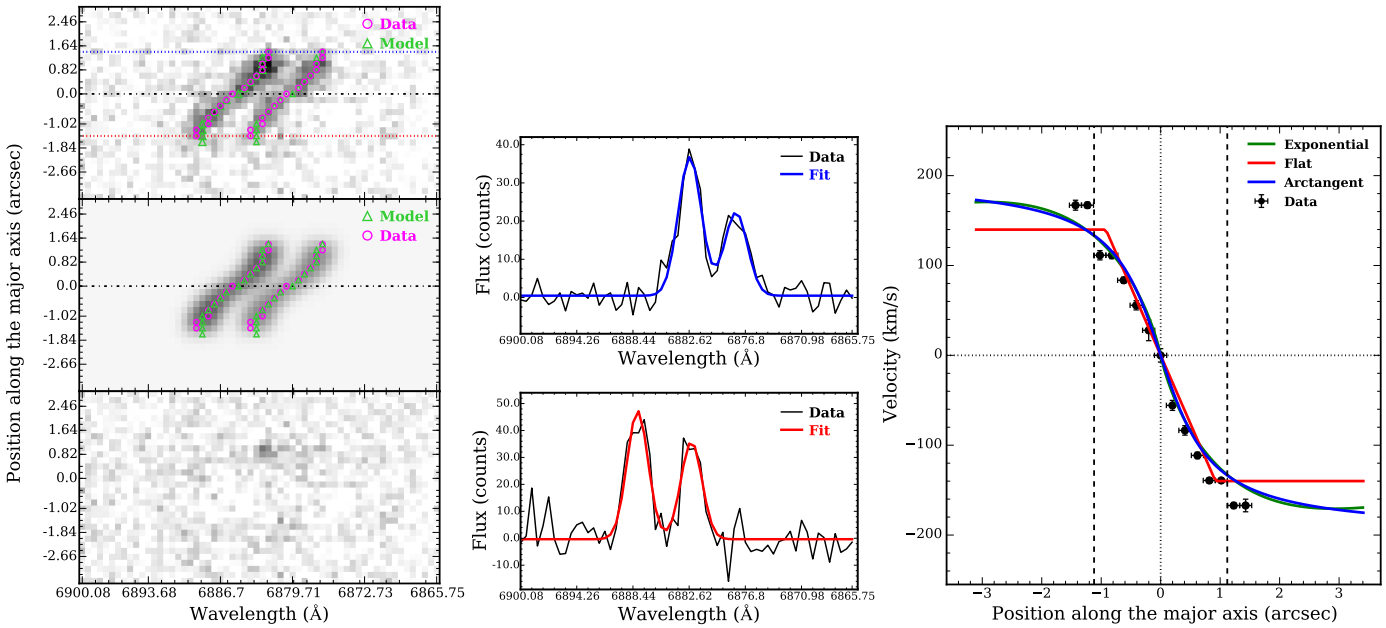

Fig. 3. Example of the output from the model-fitting process and the vision inspections to test the quality of the fit. *Left panels*: *from top to bottom*: continuum-subtracted 2D spectrum centered at [OII], best-fit kinematic model to the line emission, and residual image between the 2D spectrum and the best-fit model on the same intensity scale as the 2D spectrum. The vertical and horizontal axes are the spatial position and wavelength, respectively. In *the first two panels*, the black dot-dashed lines indicate the best-fit parameter $r_{\rm cen}$. In *the top panel*, the blue and red dotted lines denote the positions from where the plots in *the middle panels* are extracted. The 2D spectrum from the VIMOS mask has been rotated to have always the North direction in *the top*. For this reason the wavelength direction is opposite to the conventional representation with values increasing (getting redder) towards left. The technique of tracing the emission line as a function of the position (see text Sect. 3.2) is also shown in *the top and middle pannels*. Fuchsia circles show the central wavelength of the emission line at each position, and the green triangles show the centroids of the best-fit model. *Middle panels*: examples of the double Gaussian fit to measure the centroids of the emission line at two most external galaxy radii. *Right panel*: high-resolution rotation curve models (green line: exponential disc; red line: flat model; blue line: arctangent function), not corrected for the inclination, compared to the observed rotation curve (black circles). The errorbars on the y-axis direction represent the uncertainties of the fit to the line at each position to recover the centroid; the bars on the position direction indicate the bin size. The vertical dotted line indicates the galaxy rotation center, the horizontal dotted line indicates the systemic velocity, and the two vertical dashed lines indicates the position of the radius $R_{2.2}$ at which the velocity is measured to derive the scaling relations (Sect. 4.1).

Wisnioski et al. (2015), who studied the galaxy kinematics of a sample of galaxies at $0.7 \leq z \leq 2.7$ with KMOS, and have found that the agreement between photometric and kinematic PA is better than 15° for 60% of the galaxies, and for 80% of the galaxies the agreement is better than 30°, while misalignments greater than 30° typically have axis ratios $b/a > 0.6$. In our sample only 23 galaxies (out of 82) have $b/a > 0.6$.

The parameters that describe the rotation velocity $V_{\rm t}$ and $r_{\rm t}$, the velocity dispersion σ, the doublet line flux ratio $R_{\rm [OII]}$, and the exponential disc truncation radius $r_{\rm trunc}$ have been guessed tracing the continuum-subtracted emission line as a function of the spatial position. This procedure consists of fitting a Gaussian (double Gaussian with a rest-frame separation equal to 2.8 Å between the lines of the doublet) to the line profile in the wavelength direction, and it returns the values of the central wavelength, the dispersion (both converted in velocities), and flux ratio (in case of doublet) in each spatial bin. The tracing procedure terminates when the emission is no longer detected above the local noise level ($S/N < 3$), and this gives us a guess on the parameter $r_{\rm trunc}$. Each trace has been visually inspected to ensure that the fit was not influenced by spurious reduction artifacts. An example of this procedure is shown in Fig. 3 (middle panel). We defined the initial rotation velocity parameter $V_{\rm t}$ as the average value between the maximum velocities (corrected for the inclination) reached in both *approaching* and *receding* side of the galaxy and the transition radius $r_{\rm t}$ as the average between the radii at which the two maximum velocities have been first reached. For the σ, since we decided to use a constant value, this was set as the mean over the traced dispersion, after correcting it for the instrumental dispersion following Weiner et al. (2006b). The line flux ratio $R_{\rm [OII]}$ has been defined as the mean over all the line flux ratio values measured along every spatial bin.

To recover the initial parameters that describe the surface brightness, we collapsed the emission line along the spectral direction (after subtracting the continuum), obtaining a spatial profile of the emission that has been fitted with a truncated exponential disc (a sum of two truncated exponential discs in case of a doublet) convolved with the spatial resolution. As a result, we get a first guess of the parameters Σ_0 and h. Except for the i, PA and $\lambda_{\rm line}(z)$, the other parameters are let to vary freely in the fitting process for a total of eight (nine, in the case of doublet) free parameters (Σ_0, h, $r_{\rm trunc}$, $r_{\rm cen}$, $V_{\rm t}$, $r_{\rm t}$, $V_{\rm sys}$, σ, $R_{\rm [OII]}$).

3.3. Uncertainty estimation of the parameters

The fits are done by minimizing the weighted difference between the image of the 2D line emission and the 2D model of the same line. Each pixel is weighted by its inverse variance, which is computed by summing in quadrature the contribution from both the source and continuum-subtracted background. The first comes from the Poisson noise of the line-flux counts, and the second one is estimated directly from the rms fluctuation in regions where there is no object. These weights in the fit are translated into uncertainties on the parameters, computed from

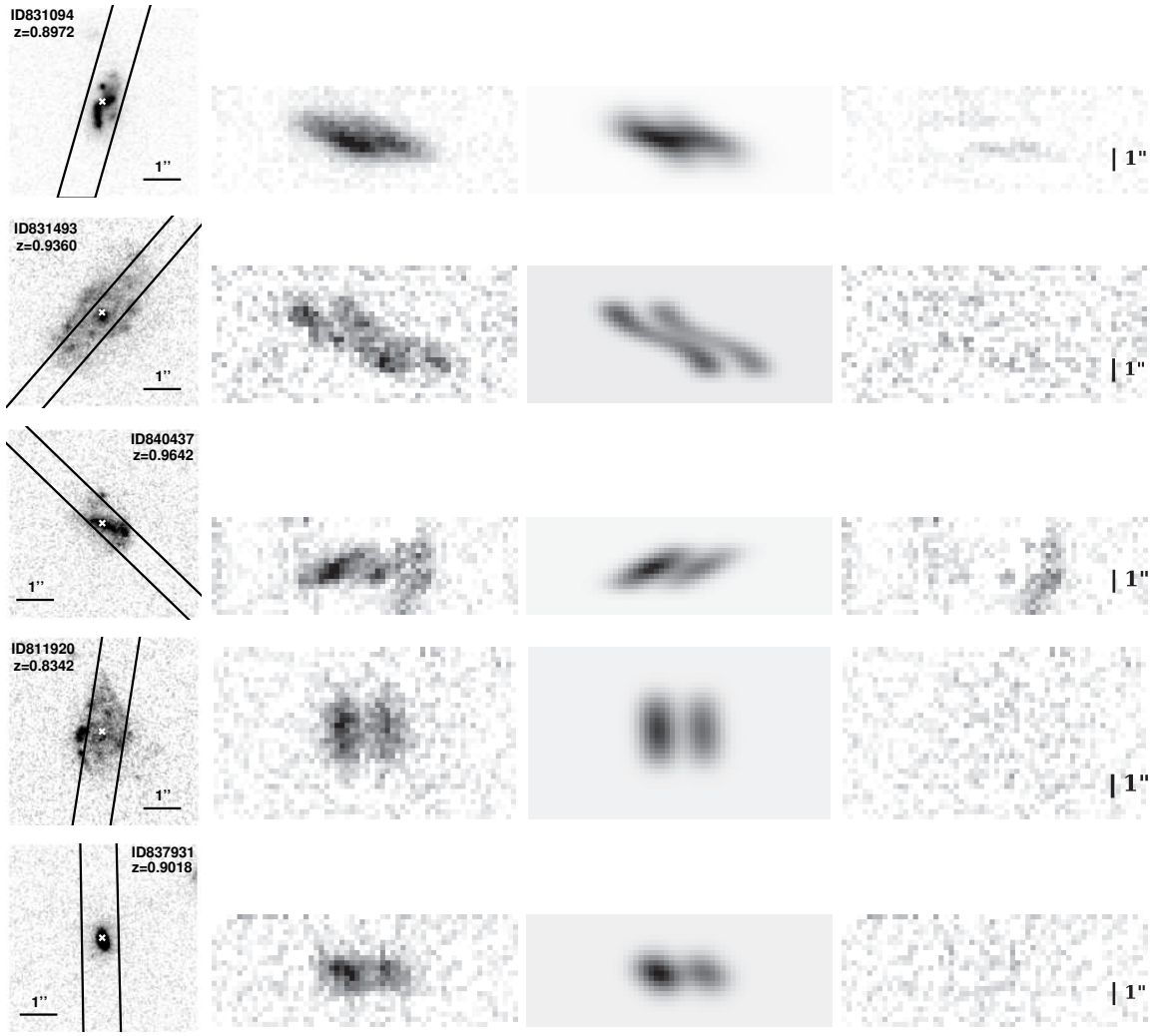

Fig. 4. Examples of galaxies from our sample. For each galaxy we show the *F814W* HST/ACS postage stamp with superimposed the 1″ width slit tilted to follow the galaxy major axis, the continuum-subtracted 2D spectrum, the best-fit kinematic model to the line emission and the residuals between the 2D spectrum and the best-fit model, on the same intensity scale as the 2D spectrum. In the spectra, the vertical and horizontal axes are the spatial position and wavelength, respectively. We show, both for the postage stamp and for the spectrum, the 1″ scale. The *first three galaxies* are classified as rotation-dominated, whereas *the other two galaxies* are dispersion-dominated.

the covariance matrix. To the 1σ formal error from the fits, we added in quadrature to error on the parameter V_t the uncertainties coming from the inclination (propagated from the uncertainties on b/a) and from the PA, since those parameters are kept fixed in the fitting process. The adopted b/a, from the Zurich Structure and Morphology Catalog, was measured with a software (GIM2D, see Sect. 2.1), which gives morphological measurements that have been corrected for the instrumental point-spread function (PSF). In Sect. A, we computed systematic uncertainties on the measurements of the axial ratio b/a derived by small variation of the PSF and added them to the velocity error budget. We measured the instrumental resolution from the sky-lines (see Sect. 2.3) and we found that it varies from 2.58 Å to 3.20 Å with a distribution that peaks at 2.63 Å. Since we constructed our model using the nominal spectral resolution (3 Å) of the instrument, we adjusted the value of the parameter σ by applying a resolution correction using the value of the peak of the spectral FWHM distribution 2.63 Å, and then we added the dispersion of the distribution to the uncertainties on σ. In median, we added $-0.8\,\mathrm{km\,s^{-1}}$ and $+4.7\,\mathrm{km\,s^{-1}}$ to the formal error on σ from the fit.

4. Results

4.1. Kinematic parameters

The Levenberg-Marquardt least-squares fitting method is known to be sensitive to the local minima, thus it is important to choose the initial guesses as being as close as possible to the global minima. We accounted for this by measuring the initial guesses as described in Sect. 3.2. Furthermore, to explore the effect of the initial guesses on the resultant models, we adopted a Monte Carlo approach, which consists of perturbing the initial guesses by sampling a Gaussian distribution, obtaining 500 combinations of the free parameters and running the fit for every single combination. Amongst the fits that converged to a best-fit solution, we discarded the ones that have obviously wrong values for the parameters and extremely high values of the parameter errors, and we pre-selected the best-fit solutions in the lowest range of χ^2 (within the 10% of the lowest value). We then defined the best-fit model as the solution with the value of the parameter V_t appeared most frequently at the most frequent χ^2 value in the pre-selected χ^2 distribution. Our results do not change if we, instead, define the best-fit model as the solution with the most

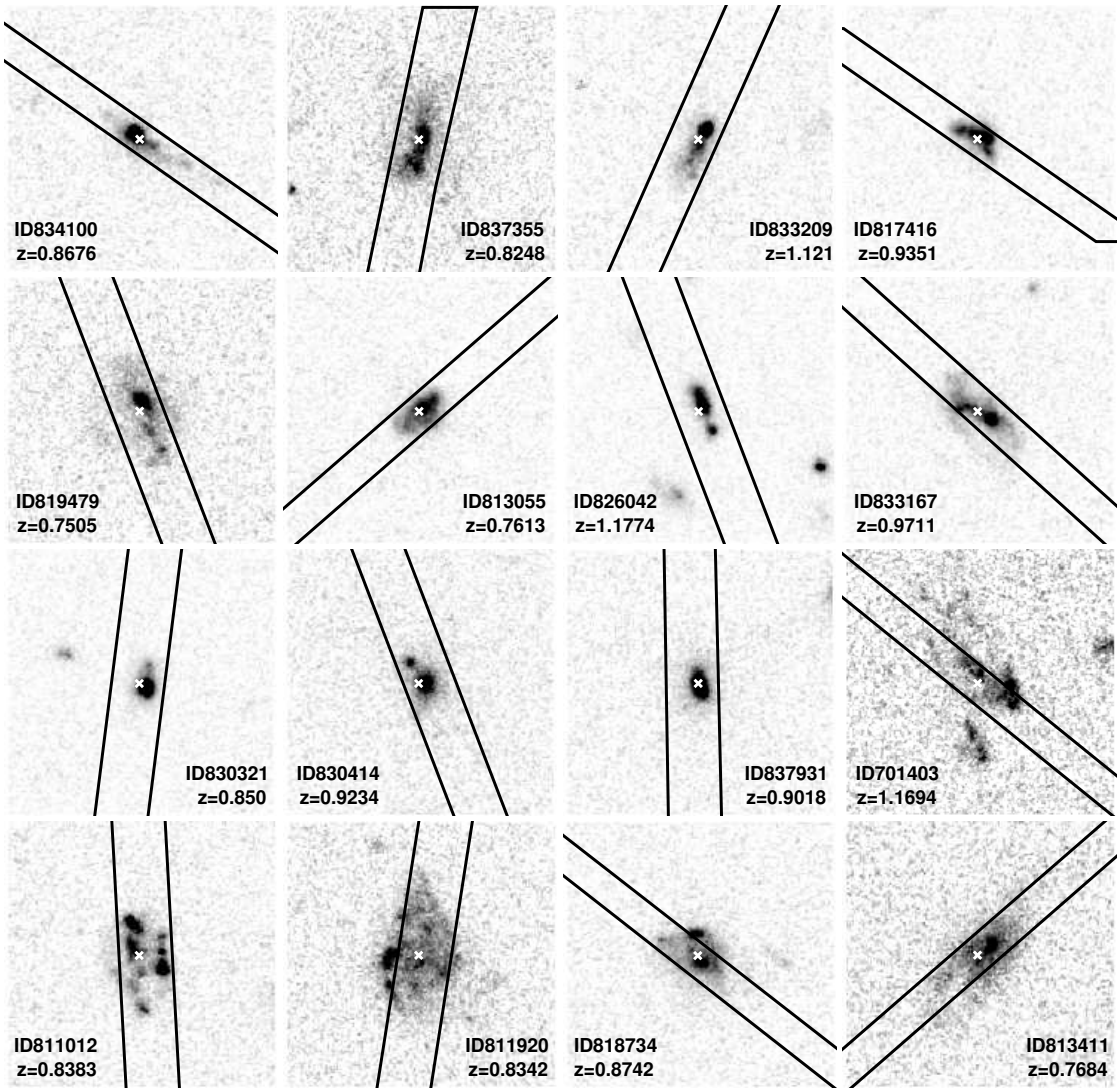

Fig. 5. *F814W* HST/ACS postage stamps of our sub-sample of dispersion-dominated galaxies, with superimposed the 1″ width slit tilted to follow the galaxy major axis.

frequently occurring value of the parameter V_t within the pre-selected χ^2 distribution.

In this way, we obtained one best solution (when available) for each modeled rotation curve (exponential disc, flat model and arctangent function). For each galaxy, we visually inspected their residual images, the trace of the emission at each position (see Sect. 3.2) – both for the observed spectrum and the modeled one – and their rotation curves (see Fig. 3). In general we chose the exponential disc solution, if available, by default. For our sample 60% of the galaxies were modeled by an exponential disc rotation curve. If the exponential disc solution was not available, we adopted the flat model solution and, if not available, the arctangent function solution. This decision was motivated by the fact that for the 50% of the sample, for which we got successfully a best-fit solution for each rotation curve model, the velocity $V_{2.2}$, that is the velocity used to derive the scaling relations (see later in this subsection), was always consistent within the uncertainties for all the rotation curve solutions.

The χ^2-minimization fitting was run for 89 galaxies. Although seven of these presented noisy spectra ($S/N < 3$), the fitting was attempted. However, from our visual check we found that no best-fit parameters could properly reproduce the observations, so we discarded them, which resulted in a final sample of 82 galaxies. Examples of ours spectral data and best-fit model are shown in Fig. 4.

To retrieve galaxy scaling relations and the dynamical masses, it is important to choose a fiducial radius at which the rotation velocity is measured. Past studies have shown that using different kinematic estimators (e.g., the maximal rotation velocity V_{max}, the plateau rotation curve velocity V_{flat}, the velocity V_{80} measured at the radius containing ∼80% of the total light, and the velocity $V_{2.2}$ measured at $R_{2.2} = 2.2\,R_d$, where R_d is the disc scale-length estimated from broad band imaging) can lead to different results (see, e.g., Verheijen 2001; Pizagno et al. 2007). In our sample, we adopted the $V_{2.2}$ estimator, which provides the tightest scatter in various galaxy scaling relations for bright galaxies and the best match to radio (21 cm) line widths for local galaxies (Courteau 1997). The values of $R_{2.2}$ are computed as 2.2 times the galaxy disc scale length measured from the HST/ACS *F814W* images (Scarlata et al. 2007) and included in the Zurich Structure and Morphology Catalog.

The model is not always able to reproduce the surface brightness profile of the observation, since a few discs are likely to be well described by an exponential profile, especially at high redshift, where a considerable number of galaxies shows clumpy star formation (Förster Schreiber et al. 2009; Wuyts et al. 2012).

We tested the reliability of rotation velocity parameters obtained from the fitting to the models by creating mock observations of galaxies (including the contribution of the background noise) with known rotation velocity and with diverse surface brightness profiles (generally described as a sum of two exponential functions with different Σ_0, r_0 and r_{cen}) and we fitted them with our models, assuming an exponential disc surface brightness. We obtained that the values of the velocity best-fit parameters with different surface brightness profiles were always consistent within 1σ errors. We also tested (see Appendix B) the correctness of the assumption of an exponential disc profile on the real data, by using an algorithm from Scoville et al. (1983; see Sect. 3 therein for a detailed description) to derive the high-resolution spatial distribution of the galaxy emission that best matches the observed emission line profile shape. Including the profile derived in this way and re-fitting to the data, we found that the rotation velocity parameters were not affected by adopting this surface brightness profile.

The kinematic parameters of our sample are listed in Table E.1. We found that in 82 successful fits, 66 galaxies (80%) are formally rotation-dominated and 16 galaxies (20%) are dispersion-dominated, by $V_{2.2}/\sigma > 1$ and $V_{2.2}/\sigma < 1$, respectively. We present in Fig. 5 HST/ACS images of our sample of dispersion-dominated galaxies. In Fig. 6 we show a correlation between $V_{2.2}$ and σ for dispersion-dominated and rotation-dominated galaxies. Each point in Fig. 6 is color–coded according to its stellar mass and we can see that the most massive galaxies amongst the rotation-dominated ones have the largest values of $V_{2.2}$. A similar result was found by Epinat et al. (2009), who have studied the kinematics of a sample of star-forming galaxies at $1.2 < z < 1.6$. This would imply that the most massive star-forming galaxies are the most kinematically settled. Same result was presented by Kassin et al. (2012), who studied the internal kinematics of 544 so called blue galaxies with stellar masses ranging $8.0 < \log M_*(M_\odot) < 10.7$ over $0.2 < z < 1.2$, and found the most massive galaxies being the most evolved at any time. Another study from Simons et al. (2015) reports a transition mass in the smTF relation, $\log M_*(M_\odot) = 9.5$, which they call the "mass of disc formation" M_{df}, for a sample of emission line galaxies at $0.1 < z < 0.375$. This mass separates the galaxies that always form discs ($M_* > M_{df}$) and are settled on to the local smTF relation, from those which may or may not form discs ($M_* < M_{df}$) and can either lie on the smTF relation or scatter off of it to low rotation velocity and higher disordered motions. We are aware, however, that the characterization of a galaxy as dispersion or rotatation-dominated is a strong function of the galaxy size. Newman et al. (2013b) compared the kinematic analysis of a sample of 81 star-forming galaxies at $z = 1.0-2.5$ using IFU data observed with both seeing-limited and adaptive optics (AO) mode, and found that small galaxies are more likely to fall in the category of dispersion-dominated galaxies because of either insufficiently resolved rotation (especially with seeing-limited observations) or as a result of the almost constant values of velocity dispersion across all galaxy sizes while the values of rotation velocity linearly increase with size. They also found that many galaxies, which were considered dispersion-dominated from more poorly resolved data, actually showed evidence for rotation in higher resolution data but, in spite of this, they found that those galaxies have different average properties than rotation-dominated galaxies. They tend to have lower stellar and dynamical masses, higher gas fractions, younger ages, and slightly lower metallicities. They suggest that these galaxies could be precursors of larger rotating galaxies, as they accrete more mass onto the outer regions of their discs.

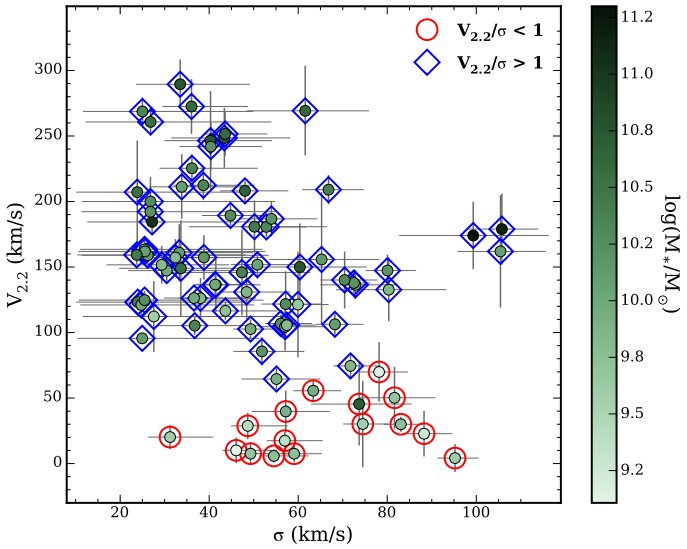

Fig. 6. Rotation velocity $V_{2.2}$ as a function of the velocity dispersion σ. The points are color–coded according their stellar mass. Blue and red circles around the points identify rotation- and dispersion-dominated galaxies, respectively.

We investigated any possible correlation between the size of the galaxies and the measured $V_{2.2}/\sigma$, by estimating the fraction of galaxies that have the radius r_{80}, defined as the semi-major axis length of an ellipse encompassing 80% of total light (from the Zurich Structure and Morphology Catalog), smaller than the measured seeing (Sect. 2.3). We found that this condition was true for 80% of the dispersion-dominated galaxies, while 60% of the total sample have r_{80} smaller than the seeing. Therefore, although r_{80} is only an approximation for the size of the galaxy, we found that the fraction of dispersion-dominated galaxies with small size is over-represented compared to the total fraction, suggesting that the classification as dispersion-dominated may be biased by the size of the galaxies.

We compared our kinematic classification to the galaxy morphologies as measured from the HST images by Scarlata et al. (2007), and we found that half of the dispersion-dominated sample is formed by galaxies defined as irregular, while 31% have an intermediate bulge and only three galaxies (19%) are classified as pure discs. The majority of the rotation-dominated galaxies, instead, are constituted of pure discs (42%), while 29% are formed by galaxies with intermediate bulge and 23% are defined as irregular. The remaining 6% is formed by three bulge-dominated galaxies and one early type. Three galaxies in Fig. 6 do not follow the correlation and, even though they rotate quite fast, they exhibit high velocity dispersion. For the two most massive galaxies a clear presence of a prominent bulge in the HST images, or unresolved inner velocity gradient not described by simple models or intrinsic dispersion, may be the cause of the high dispersion, even though their discs are still rotating. The less massive one has a bright clumpy region in the periphery, which may have high dispersion and which, due to its relatively high brightness, may dominate the emission.

Most of our kinematic sample is composed of [OII] emission line galaxies (79 out of 82) and, for those galaxies, we measured the line ratio $R_{[OII]}$ from the model fitting. We show the distribution of $R_{[OII]}$ along with its relationship to other galaxy parameters (σ, M_*, SFR) in Appendix C. We measured the rest-frame equivalent width (EW) and computed the SFR from [OII] following Lemaux et al. (2014). The choice of using EW([OII]) to

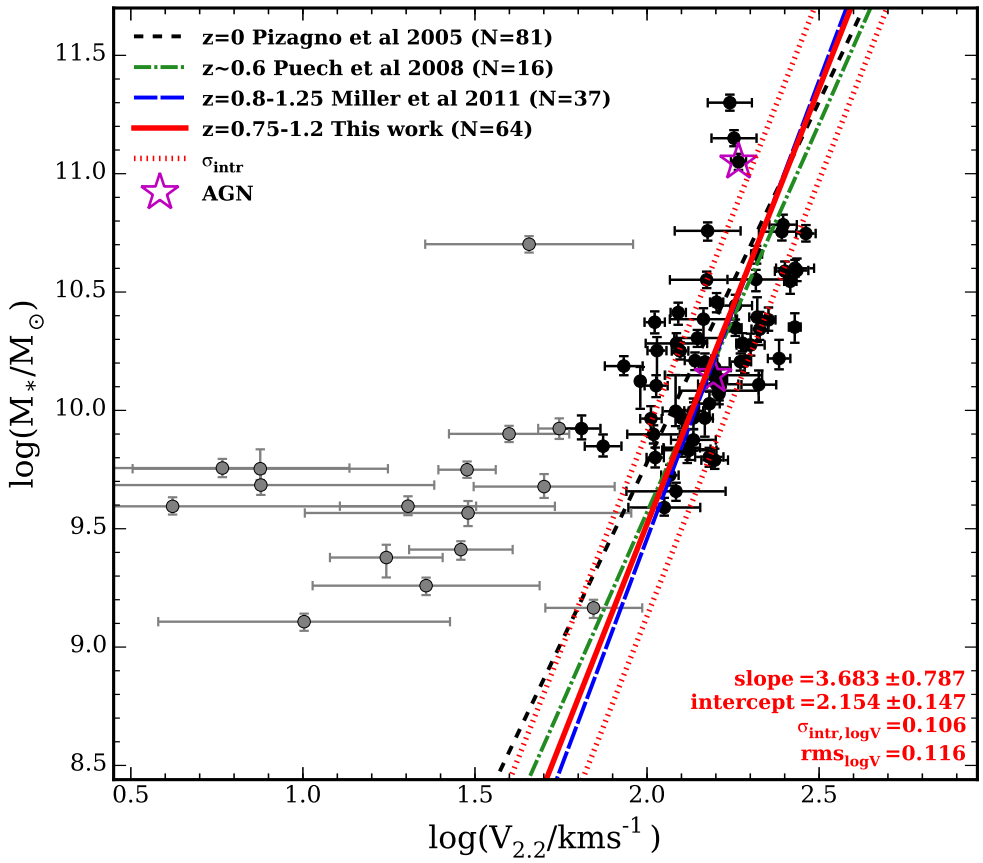

Fig. 7. SmTF relation constrained for our sample of rotation-dominated galaxies (black circles). The gray points are the dispersion-dominated galaxies. The magenta stars show the AGNs. Our fit is represented with a solid red line. The dotted red lines show the intrinsic scatter $\sigma_{\rm intr}$. We plot as references the relations at $z = 0$ (Pizagno et al. 2005) with a short-dashed black line, $z \sim 0.6$ (Puech et al. 2008) with a dot-dashed green line and $z = 0.8$–1.25 (Miller et al. 2011) with a long-dashed blue line.

derive the SFR instead of [OII] flux was motivated by the lack of the absolute flux calibration for our spectroscopic observations (see Sect. 2.3). In Fig. C.4 we show the comparison between the SFR computed using the spectral energy distribution (SED) fitting and the [OII] emission. The values of $R_{\rm [OII]}$, $SFR_{\rm SED}$ and $SFR_{\rm [OII]}$ are listed in Table E.2.

4.2. Stellar mass Tully-Fisher relation at $z \sim 0.9$

We present the stellar mass Tully-Fisher (smTF) relation obtained at $z \sim 0.9$ in the COSMOS field. This is shown in Fig. 7 and takes the form:

$$\log M_* = a\,(\log V_{2.2} - \log V_{2.2,0}) + b\,, \tag{9}$$

where a and b are the slope and the y-intercept of the relation, respectively, and $\log V_{2.2,0}$ is chosen to be equal to 2.0 dex to minimize the correlation between the errors on a and b (Tremaine et al. 2002). Since the smTF relation is known to be valid for rotating galaxies, we decided to fit the relation for the rotation-dominated sub-sample, shown in Fig. 7 with black circles, whereas the dispersion-dominated galaxies are plotted as gray points. We decided not to include the two galaxies known to be NL AGNs in the fit of the smTF relation, since we cannot tell if the emission is dominated by the AGN or by the host. We note that, for those galaxies, the stellar mass measurements may not be correct since AGNs were not taken into account in the SED-fitting process. The relation in Eq. (9) is obtained using MPFITEXY routine (Williams et al. 2010), which adopts a least-squares approach accounting for the uncertainties in both coordinates and incorporates the measurement of the intrinsic scatter $\sigma_{\rm intr}$ on the velocity variable, added in quadrature to the overall error budget. The MPFITEXY routine depends on the MPFIT package (Markwardt 2009). Following previous analyses of the Tully-Fisher relation (see e.g., Verheijen 2001; Pizagno et al. 2005, 2007; Miller et al. 2011; Reyes et al. 2011), we fitted an *inverse* linear regression to our data, where velocity is treated as the dependent variable. The relation is then inverted to compare the fitted parameters to other works, which show the *forward* best-fit parameters of the smTF relation. MPFITEXY automatically handles the inversion of the results and the propagation of errors. Forward and Inverse fitting is only symmetric if there is no intrinsic scatter ($\sigma_{\rm intr} = 0$) (Tremaine et al. 2002), but generally this is not the case. It has been shown in previous works (e.g., Willick 1994; Weiner et al. 2006a) that there is a significant bias in the slope of the forward best fit relation introduced by the sample selection limits. Therefore the inverse relationship is usually preferred, where the galaxy parameters that are more subject to the selection effects (magnitude, stellar mass) are treated as the independent variable.

We determined the 1σ errors on a, and b, by repeating the fit for 100 bootstrap sub-samples of 82 galaxies from the full rotation-dominated galaxy sample and taking the dispersion of the distribution of bootstrap estimated parameters as the uncertainty in the same parameters. Our best-fit parameters are shown in Table 2.

To investigate the evolution of the smTF relation with redshift, we plotted the relations at $z = 0$ from Pizagno et al. (2005)

Table 2. Stellar mass Tully-Fisher parameters.

a	b	$\sigma_{\mathrm{intr,\,log}\,V}{}^{i}$	$\mathrm{rms}_{\mathrm{log}\,V}{}^{i}$	$\delta_{\mathrm{med,\,log}\,V}{}^{i}$	$\sigma_{\mathrm{intr,\,log}\,M_*}{}^{ii}$	$\mathrm{rms}_{\mathrm{log}\,M_*}{}^{ii}$	$\delta_{\mathrm{med,\,log}\,M_*}{}^{ii}$
3.683 ± 0.787	2.154 ± 0.147	0.106	0.116	0.043	0.389	0.425	0.043

Notes. Best-fit parameters of the smTF relation, expressed as $\log M_* = a\,(\log V_{2.2} - \log V_{2.2,0}) + b$, where $\log V_{2.2,0} = 2.0$ dex is the "pivot" value adopted to minimize the correlation between the errors on a and b. The forward parameters are obtained by inverting the best-fit parameters from the inverse fit. The slope of the relation is a and b is the y-intercept. σ_{intr}, rms and δ_{med} are the intrinsic scatter, the total scatter and the median error, respectively, for both the velocity and stellar mass in logaritmic units. $^{(i)}$ dex in $V_{2.2}$; $^{(ii)}$ dex in M_*.

and at $z \sim 0.6$ from Puech et al. (2008). A smTF relation in similar redshift range to our sample ($0.8 < z < 1.25$) was presented by Miller et al. (2011) for 37 galaxies in the GOODS fields and we also plotted it for comparison. Our result shows no significant evolution with redshift and it is in good agreement with the result obtained by Miller et al. (2011). We also fitted the smTF relation, fixing the slope to the $z = 0$ relation form Pizagno et al. (2005) and we quantified an offset of $\Delta M_* = -0.1$ dex that is within 1σ error on the y-intercept and is consistent with the no significant evolution observed by Miller et al. (2011; $\Delta M_* = -0.037$ dex) and by the predictions from the cosmological simulations up to $z = 1$ (Portinari & Sommer-Larsen 2007). Conversely, Puech et al. (2008) found an offset of the smTF relation at $z \sim 0.6$ equal to $\Delta M_* = -0.36$ dex with respect to the local relation, suggesting an evolution of the smTF relation. Small differences in the slope that we measured compared to Pizagno et al. (2005) and Puech et al. (2008) may arise from different adopted techniques used to compute galaxy stellar mass and, in particular, from the IMF assumption. Indeed, the former assumed a Kroupa IMF (Kroupa 2001) and the latter a "diet-Salpeter" IMF (Bell & de Jong 2001; Bell et al. 2003). Miller et al. (2011), conversely, assumed a Chabrier IMF, as we did.

A recent work on the TF relation at $z \sim 1$ from the KROSS survey, using the multi-object IFU KMOS, has been presented by Tiley et al. (2016). They constrained the smTF and K-band TF relations for a sample, denoted as "disky", of 56 rotation-dominated galaxies (out of 210 galaxies with well-measured rotation velocity) at $z = 0.8-1.0$, applying the strict selection criterion $V_{80}/\sigma > 3$. They computed stellar masses assuming Chabrier IMF. They found evidence of significant evolution of the smTF relation towards lower masses, $\Delta M_* = -0.41$ dex, while no evolution in the K-band TF relation. This result is very different from the one we found both on the slope (their relation has a slope of a value 4.7) and on the evidence of evolution of the relation, despite the fact that we also selected galaxies dominated by the rotation to constrain the smTF relation but with a less stringent cut ($V_{2.2}/\sigma > 1$). Tiley et al. (2016) stress the importance of their result, obtained by selecting strictly rotation-dominated galaxies, to make the comparison with TF relations for $z \sim 0$ late-type galaxies that are dominated by the rotation. They argue that the difference with past works, which found no evolution of the smTF relation (Conselice et al. 2005; Miller et al. 2011), is due to the inclusion of galaxies with low ratios of rotation-to-pressure support. We find that the cut applied by Tiley et al. (2016) to keep galaxies only supported by the rotation is overly strict and probably it introduces a bias in their "disky" sample which removes all the galaxies with velocity smaller than $\sim$120 km s^{-1} (except for one galaxy with 84 km s^{-1}) for stellar masses between $10^{8.9}\,M_\odot$ and $10^{11}\,M_\odot$. In our kinematic sample, conversely, 12 galaxies have $V_{2.2} < 120$ km s^{-1} with a minimum value of 64 km s^{-1}. Some of the galaxies used by these authors have been observed in the COSMOS field and we may have some targets in common but, unfortunately, we were not able to recover the coordinates of these galaxies to make a direct comparison.

Our smTF relation shows an intrinsic scatter of 0.106 dex in velocity. This is smaller than the value obtained by Puech et al. (0.12 dex), but it is larger than the scatter obtained by Pizagno et al. (2005) and Miller et al. (2011; $\sim$0.05 dex for both). An important factor, which influences the scatter, is the measurement of the errors since σ_{intr} is computed assuming that the uncertainty estimation is correct. Therefore the details of how the analysis is actually carried out have a very strong effect on the result. Another factor that definitely affects the scatter around the smTF relation is the sample selection. Kannappan et al. (2002) have shown that the scatter around the TF relation increases by broadening their spiral sample, for which the relation is computed, to include all morphologies. They also argue that local studies tend to weed out kinematically irregular galaxies; therefore if a more representative sample of spirals is selected, the scatter could actually be much higher. At intermediate redshifts, small irregularities in rotation curves are harder to detect, owing to limited spatial resolution, and so a higher measured scatter might reasonably be expected (Moran et al. 2007). We emphasize that our sample was not subject to a pre-selection that aims to prefer some galaxy morphologies rather than others, and that our selection on the inclination and the PA was driven only by the necessity to create the observing conditions that favor the extraction of the kinematics information. Moreover, the selection based on the GINI parameter (Sect. 2.1) was applied to a small fraction of our sample (17%), for which we did not have prior spectroscopic information. In fact, the whole sample spans a wide range of GINI parameters from 0.29 to 0.60. Conversely, Pizagno et al. (2005) applied a strict morphological cut in their sample, selecting galaxies with a disc-to-total luminosity ratio greater than 0.9, and Miller et al. (2011) made a morphological selection favoring disc-like structures, even though they attempted to avoid to favor "well-behaved" spirals and included a more morphologically disturbed population in their sample. We conclude that we do not have the conditions to investigate the evolution of the scatter with redshift. Therefore, rather than comparing the scatter with other studies that have different selections, we opt to internally compare our own data from the overall sample as a function of redshift in a future work.

Knowing that M_* and $V_{2.2}$ are not measured at the same radius, to ensure consistency of our smTF relation and that the comparison with other works is fair, we repeated the fit of the relation following the technique adopted by Miller et al. (2011). In one case, we constrained the relation for stellar masses and velocities, both measured at the radius $R_{2.2}$. To that end, we applied an aperture correction to the stellar mass by estimating the fraction of light contained within $R_{2.2}$ for an exponential profile galaxy (see Sect. 4.3). In the other case, we derived the smTF relation using the total stellar mass of our galaxies and the velocity measured at the radius $R_{3.2}$, also called optical radius, which

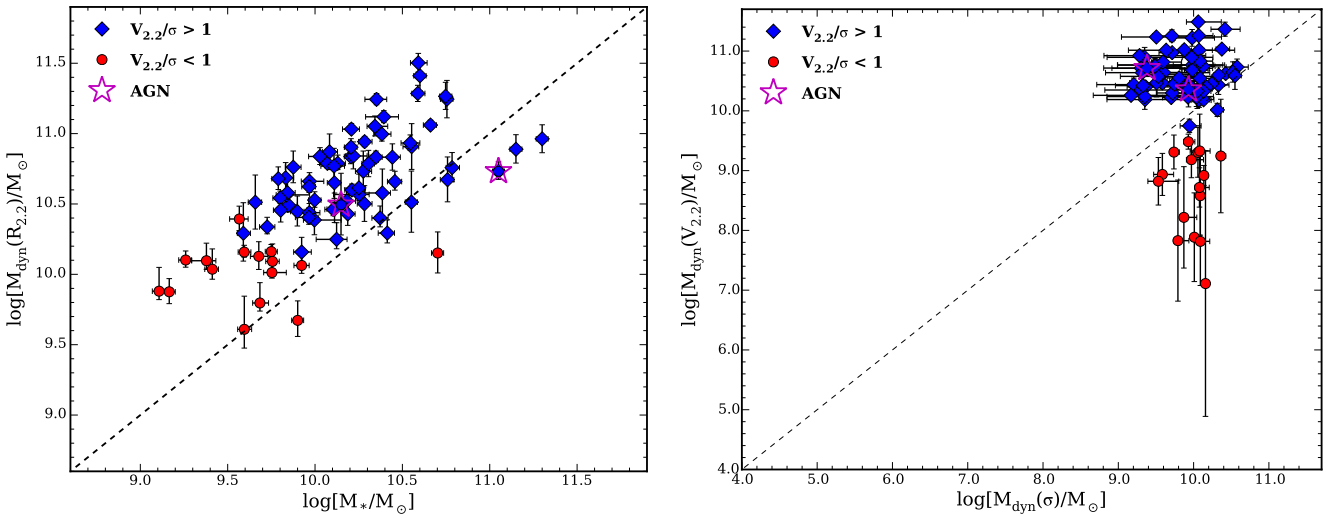

Fig. 8. *Left panel*: comparison between dynamical (y-axis) and stellar (x-axis) masses in logarithmic units. Blue diamonds and red circles represent the rotation- and dispersion-dominated galaxies, respectively. The magenta stars show the AGNs. The dashed line represents the relation 1:1. *Right panel*: rotation versus dispersion contributions to the $M_{\rm dyn}$. Blue diamonds and red circles are the rotation- and dispersion-dominated galaxies, respectively. The magenta stars show the AGNs. The dashed line represents the relation 1:1.

contains 83% of the total integrated light and, for an exponential disc, is equal to 3.2 times the disc-scale length. In both cases, the smTF relation is in good ($\lesssim 2\sigma$) agreement with the relation presented in Fig. 7 for the best-fit value of slope and y-intercept. We find, moreover, that the relation computed at the radius $R_{2.2}$ exhibit the same intrinsic scatter ($\sigma_{\rm intr} = 0.106$ dex) as our original relation, while the relation derived at $R_{3.2}$ shows a larger intrinsic scatter ($\sigma_{\rm intr} = 0.128$ dex), most likely due to the fact that the emission of most of our galaxies does not extend that far out and the measurements of the velocity at $R_{3.2}$ are the result of an extrapolation at that radius. We are therefore confident that the comparison with other works of the smTF relation derived in our study is not subject to bias introduced by the different radii at which M_* and $V_{2.2}$ are measured.

4.3. Dynamical mass measurements

In this section, we present the dynamical masses computed for our sample of star-forming galaxies at $0.75 < z < 1.2$. The dynamical mass of disc galaxies is defined by the maximum rotation velocity following the formula

$$M_{\rm dyn}(R) = \frac{V_{\rm ROT}^2\, R}{G}\,, \tag{10}$$

where R is the radius at which we measure the maximum velocity and G is Newton's gravitational constant. However, this formula is valid for galaxies with total mass that is supported mainly by the rotation and, as we have shown in Sect. 4.1, our sample is 20% composed of dispersion-dominated galaxies, for which the measured slow rotation is not enough to dynamically support the galaxy mass. For these galaxies, to take into account the pressure support, we apply an "asymmetric drift correction" term (Meurer et al. 1996), which involves radial gradients of the gas surface density, the gaseous velocity dispersion, and the disc scale-height. We assumed that (i) the galaxy kinematics is axisymmetric; (ii) the gas velocity dispersion is isotropic; (iii) the velocity dispersion and the scale-height of the galaxy disc are constant with radius; and (iv) the gas surface density profile follows the exponential galaxy surface brightness, assumed in our models (Eq. (2)). Adapting the equation (2) from Meurer et al. (1996) for an exponential gas surface density profile, we computed the asymmetric drift correction, which leads to the following expression of the dynamical mass within $R_{2.2}$:

$$M_{\rm dyn}(R_{2.2}) = M_{\rm dyn}(V_{2.2}) + M_{\rm dyn}(\sigma) = \frac{V_{2.2}^2\, R_{2.2}}{G} + \frac{2.2\sigma^2 R_{2.2}}{G}\cdot \tag{11}$$

The two terms of Eq. (11), $M_{\rm dyn}(V_{2.2})$ and $M_{\rm dyn}(\sigma)$, refer to the rotation and dispersion contribution to the total mass, respectively. The first term, $M_{\rm dyn}(V_{2.2})$, represents the mass enclosed within the radius $R_{2.2}$, the second term, $M_{\rm dyn}(\sigma)$, represents the asymmetric drift correction at the same radius. The dynamical mass of each galaxy is given in Col. (12) of Table E.1, the uncertainties are estimated by the propagation of the errors on $V_{2.2}$ and σ. The values range between $2.5 \times 10^9\, M_\odot$ and $2.3 \times 10^{10}\, M_\odot$ with a median value of $1.0 \times 10^{10}\, M_\odot$ for the dispersion-dominated galaxies, and between $1.3 \times 10^{10}\, M_\odot$ and $3.1 \times 10^{11}\, M_\odot$ with a median value of $4.5 \times 10^{10}\, M_\odot$ for rotation-dominated galaxies.

In Fig. 8 (left panel), we present the comparison between the computed dynamical mass and the stellar mass (Sect. 2.4). We find that our independent measurements of stellar and dynamical mass have highly significant correlation. The dynamical mass gives us a measure of the total mass of the galaxy within the radius $R_{2.2}$, including all its components (stars, gas, and dark matter). Therefore, as expected, $M_{\rm dyn}(R_{2.2})$ is generally equal to or greater than M_*. Within their uncertainties, a few galaxies have $M_* > M_{\rm dyn}(R_{2.2})$.

Knowing that both masses, M_* and $M_{\rm dyn}$, are measured at different radii (M_* is evaluated at larger radius), to make a comparison with previous works, we computed an aperture correction by estimating the fraction of light contained within $R_{2.2}$ for an exponential profile galaxy. We found that 65% of the total *F814W* light is included in $R_{2.2}$ and we have applied this correction to M_* measurements. We computed the stellar-to-dynamical mass fraction within $R_{2.2}$ for our sample, and we found a median value of 0.2, which means that the contribution from gas+dark matter masses is 80% of the total dynamical mass within $R_{2.2}$. Our stellar-to-dynamical mass fraction is consistent with the fraction measured by Stott et al. (2016) within $R_{2.2}$ for star-forming galaxies at $z = 0.8-1.0$ from the KROSS

survey. They found that, on average, 78% of the total mass within $R_{2.2}$ is composed of non-stellar material. Miller et al. (2011) obtained a value of stellar-to-dynamical mass fraction within $R_{2.2}$, across all their sample at $0.2 < z < 1.3$, equal to ~0.3 with a considerable scatter ($\sigma_{\rm int} = 0.25$), while Wuyts et al. (2016) found a median fraction equal to 0.32 within the H-band half-light radius for a sample of star-forming discs from the KMOS^{3D} survey, spanning a wide redshift range of $0.6 < z < 2.6$. We note that the stellar-to-dynamical mass fraction is dependent on the IMF assumed when computing the stellar mass. Assuming, for example, a Salpeter IMF (Salpeter 1955), the stellar-to-dynamical mass fraction would have been equal to ~0.33, since galaxy stellar masses calculated assuming a Chabrier IMF are ~0.6 times smaller than the ones calculated assuming a Salpeter IMF. For the comparison with previous works, the studies discussed here have computed stellar masses assuming Chabrier IMF.

Figure 8 (right panel) presents the rotation versus the dispersion contributions to the $M_{\rm dyn}$. Here we see, even more clearly than in Fig. 6, the separation between rotation- and dispersion-dominated galaxies.

4.4. SmTF relation as a function of the environment

Another important question we are trying to answer is: does the smTF relation have any dependence on the environment? Usually galaxy parameters vary according to the environment in which they are located (Baldry et al. 2006; Bamford et al. 2009; Capak et al. 2007; Sobral et al. 2011; Scoville et al. 2013), hence we expect to observe this dependence reflecting in the galaxy scaling relations. To investigate possible variations of the smTF relation we first defined environments by using the local surface density measurements by Scoville et al. (2013) in the COSMOS field. They used the two-dimensional Voronoi tessellation technique (Ebeling & Wiedenmann 1993) to measure the local density ($\Sigma_{\rm vor}$) associated with each galaxy, and to map and visualize coherent the large-scale structure for a $K_{\rm S} \leq 24$ sample of 155 954 galaxies out to $z = 3$, using extremely well-constrained photometric redshifts. Darvish et al. (2015) have shown, with extensive simulations on evaluating the performance of different density estimators, that the Voronoi tessellation technique (along with adaptive kernel smoothing technique) outperforms other methods and thus it should be considered as more reliable and robust than the widely-used nearest-neighbor (usually 5th or 10th NN) or count-in-cell (CC) techniques.

To attempt other environment measurements we searched in group catalogs available for the COSMOS field to determine if an appreciable number of galaxies in our sample had been classified as group members. We looked at a catalog of X-ray selected groups from George et al. (2011) and found that only one galaxy in our sample was defined as a member of a poor ($N_{\rm mem} < 3$) group. The percentage of our selected galaxies that are classified as group members is 1%, hence smaller than the 3% found for the galaxies part of the X-ray selected groups catalog at $0.75 < z < 1.2$. Another group catalog was built by Knobel et al. (2012), based on spectroscopic redshift measurements in the zCOSMOS-bright survey. We found that only 18 galaxies of our sample are present in their catalog, of which 13 have a significant probability of being associated to a group. We note that the work of George et al. (2011) presents inconsistencies with Knobel et al. (2012). Owing to a low number of our galaxies in group catalogs and to the inconsistency between these two works, we use the local density measurements to define the environment and we defer to future works to proper define other environment measurements.

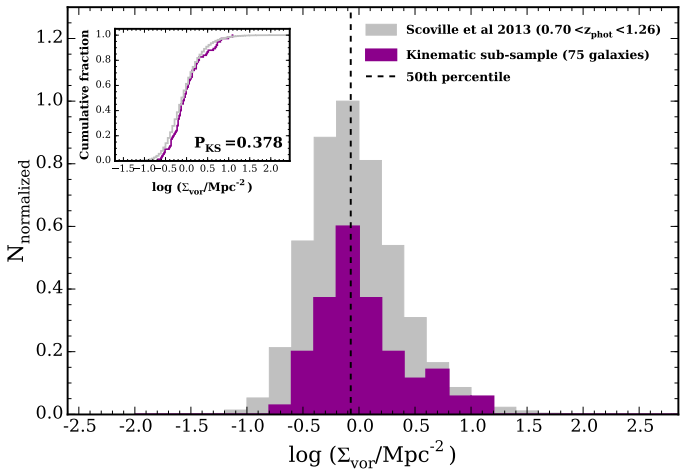

Fig. 9. Local density distributions. The gray histogram represents the distribution of $\log_{10}(\Sigma_{\rm vor}/{\rm Mpc}^2)$ for the parent galaxy sample from Scoville et al. (2013) at $0.75 < z < 1.2$. The purple histogram shows the density distribution of our sample. Both histograms are re-normalized for a better visual comparison of their spreads and peaks, therefore their normalization does not reflect the actual scale. The vertical line splits in half the parent local density distribution, to define the low- (to the left) and the high- (to the right) density environments. The *plot embedded* shows the comparison of the two cumulative distributions of both samples with the resulting value from the K-S test.

In Fig. 9, we show the density distribution of the parent galaxy sample from Scoville et al. (2013) at $0.75 < z < 1.2$ and the density distribution of our galaxy sample. In the parent sample, seven of our galaxies do not have density measurements and, therefore, will not contribute to our investigation. Since we are not interested in comparing the normalization of the distributions, we re-normalized the histograms to better visually compare their spreads and peaks (their normalization does not reflect the actual scale). To quantify any bias between the two samples we performed a Kolmogorov-Smirnov (K-S) test. We defined a null hypothesis that both samples are drawn from the same distribution and we rejected the null hypothesis if the p-value $P_{\rm KS}$ is below the value 0.05. We find that both samples are consistent with having been drawn from the same distribution ($P_{\rm KS} = 0.38$).

We defined low- and high-density environments such that the parent local density distribution in the redshift range of our interest was split in half. A first attempt to divide the overall distribution in three environmental density bins – low, moderate, higher density – have been made based on projected density quartiles and interquartile, but we have too low statistical significance in two of the three bins. Therefore we decided to increase the statistic significance and to consider two environment classes. The low-density environment has values of $\log_{10}(\Sigma_{\rm vor}/{\rm Mpc}^2)$ between −0.678 and −0.074 and the high-density environment has values between −0.074 and 1.113 $\log_{10}(\Sigma_{\rm vor}/{\rm Mpc}^2)$. As we see in Fig. 9, the local density distribution of our sample does not reach the lowest nor the highest value of the parent distribution. Our galaxies do not probe the least dense environments (void-like regions) in the COSMOS field nor the most dense ones typical to cluster galaxies, hence our sample is characterized by a local density distribution that goes from a slightly less dense environment than field galaxies to group galaxies.

We plotted our smTF relation for galaxies in lower (pink diamonds) and higher (purple squares) density environments in the top panel of Fig. 10. Here we investigate the possibility that any correlation exists between the scatter of the galaxies around the relation (even for the dispersion-dominated ones) and their environment, in order to understand if the environment can influence the galaxies so that they deviate from the scaling relation. Visually we do not detect any difference in the spread of the two galaxy sub-samples around the relation computed for the rotation-dominated galaxies (Sect. 4.2). To properly quantify the difference in scatter between the galaxies in both density environments, we define a quantity d_w as the 1σ error weighted shortest distance to the relation between our data points and the smTF relation. We introduced this quantity to investigate environmental effect on both rotation velocity and stellar mass. We explain in detail how d_w is computed in Appendix D. Figure 10 (middle panel) presents the distribution of the distances d_w for the full sample and for both sub-samples at low- and high-density. We see that galaxies in the two environments have remarkably similar distributions to that for the full sample. In the bottom panel of Fig. 10, we compare the cumulative distributions of the galaxies in low- and high-density environments. A K-S test between them tells us that the probability that the two samples are consistent with having been drawn from the same distribution is ∼71%. This implies no difference owing to the environment in the scatter around the smTF relation. Furthermore, we explored whether any effect of the environment exists in constraining the smTF relation and we again fitted the relation, separately, for rotation-dominated galaxies in low- and high-density environments, with the slope set to the value found for our whole rotation-dominated sample. We find no significant offset of the relation ($\Delta M_* = -0.04$ dex for the sub-sample at low-density, $\Delta M_* = +0.02$ dex for the sub-sample at high-density), which is consistent with no environmental effect.

4.4.1. Previous studies

In this study, we present our investigation of the dependence of the stellar mass Tully-Fisher relation with the environment at $z > 0$, for the first time, using local density measurements obtained with the 2D Voronoi tessellation technique that identified large scale structure in the ∼2 deg^2 COSMOS field. This approach for tracing the environment makes use of the local number density of galaxies as a proxy for their host region. The conventional method to define the environment as two extreme regions in the density distribution of galaxies, i.e. galaxy cluster and general field, is an overly coarse binning of the full dynamical range of the density field at these redshifts. There are, indeed, intermediate environments, such as galaxy groups, outskirts of clusters, and filaments that are equally important (Fadda et al. 2008; Porter et al. 2008; Tran et al. 2009; Coppin et al. 2012; Darvish et al. 2014, 2015). Previous works on constraining the B-band TF relation for cluster and field galaxies at $0 < z < 1$ (e.g. Ziegler et al. 2003; Nakamura et al. 2006; Jaffé et al. 2011; Bösch et al. 2013) have found no dependence of the TF relation with environment, while other studies by Bamford et al. (2005) and Moran et al. (2007) have found this kind of change. Bamford et al. (2005) derived a B-band TF relation for 58 field galaxies at $0 \lesssim z \lesssim 1$ and for 22 cluster galaxies at $0.3 \lesssim z \lesssim 0.85$ and have found that the cluster galaxies relation is offset from the one for the field galaxies by $\Delta M_B = 0.7 \pm 0.2$ mag. Moran et al. (2007) computed the scatter around the Ks-band (proxy of the stellar mass) and V-band TF relations at $0.3 \lesssim z \lesssim 0.65$ for 40 cluster galaxies and 37 field

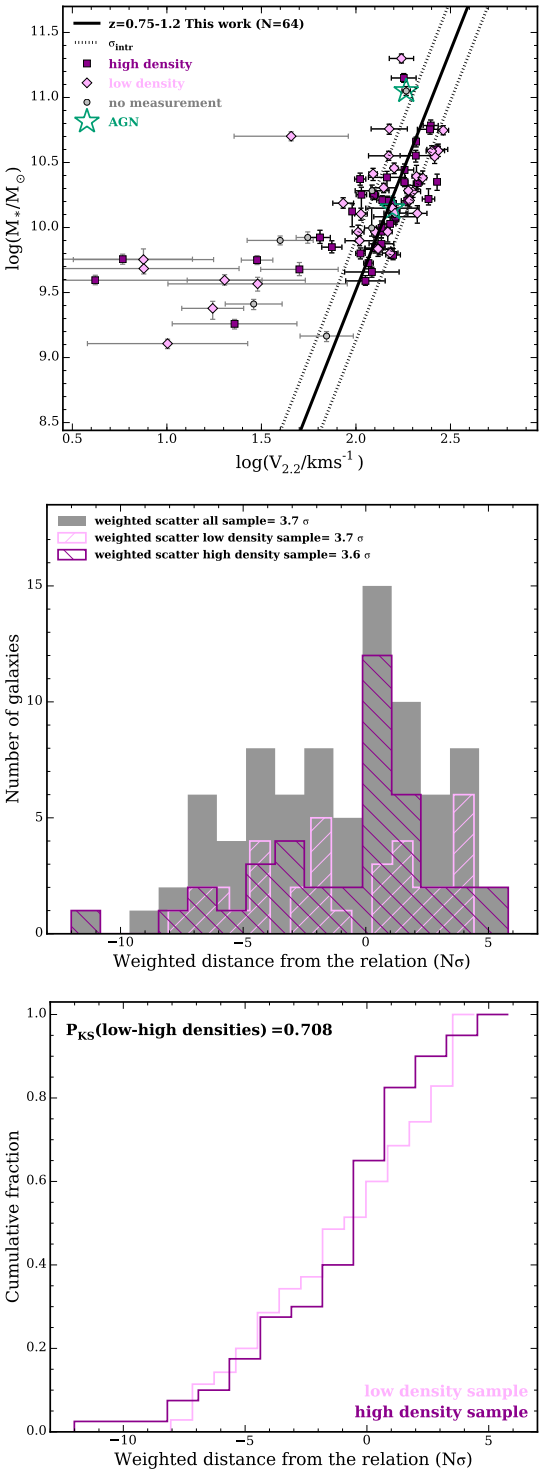

Fig. 10. *Top panel*: stellar mass M_* versus rotation velocity $V_{2.2}$ for our sample at $0.75 < z < 1.2$ in different environments. The pink diamonds and the purple squares are for galaxies in lower and higher density environment, respectively. The gray circles are the galaxies for which we do not have density measurements. The green stars identify the AGNs. The black solid and dotted lines show our smTF relation with the intrinsic dispersion. *Middle panel*: distribution of the 1σ error weighted distance d_w of the data points from the relation for the entire sample in gray solid histogram, and for the galaxies in low- and high-density environments in pink and purple hashed histograms, respectively. The value of the weighted scatter around the relation for the whole sample and the two sub-samples is also shown. *Bottom panel*: cumulative distribution of d_w for low (pink) and high (purple) density environment and the result of the K-S test.

galaxies, showing that cluster galaxies are more scattered than the field ones. As already pointed out, the most dense environment that our galaxies sampled is a group-scale one, therefore we cannot assert agreement or disagreement with those previous works, since they focus on comparison between field and cluster galaxies. Jaffé et al. (2011) included group galaxies in their sample and have found no correlation between the scatter around the B-band TF and the environment, nevertheless they did not explore the environmental effect on the smTF relation.

In the local Universe ($z \ll 0.1$), Torres-Flores et al. (2010, 2013) compared the kinematics of a galaxy sample composed of nearby groups from the sample of Hickson (1993) and concluded that the behaviour of most compact group galaxies on the different TF relations (B-band, K-band, stellar and baryonic) do not fundamentally differs from those shown by field galaxies. They argue, however, that the larger scatter around the relation for the compact group galaxies and the presence of some outliers indicate subtle, but intrinsic, differences between compact group and field galaxies, which may be linked to transient evolutionary phenomena owing to the dense environment of compact group of galaxies. We expect, therefore, that a galaxy that lies in a dense environment would be affected by the gravitational potential created by the surrounding galaxies and have its gas and its kinematics disturbed. In our high-density subsample, we find no such evidence of kinematic disturbances relative to the low-density sub-sample. This may be an effect of the limited dynamic range of densities probed by our sample and by the COSMOS field as a whole, an effect of combining galaxies in field and group environments in the high-density bin, a true similarity between the two populations, or some combination of the three. Within nearby cluster galaxies, it has been shown by Amram et al. (1993) that the kinematics of cluster members is not perturbed until the optical radius, while Torres-Flores et al. (2014) have found that in structures only as dense as local compact groups, a high fraction of galaxies do present significant kinematic disturbance. Jaffé et al. (2011), at $0.36 < z < 0.75$, also computed the fraction of kinematically disturbed galaxies f_K in field, group and cluster environments and they have obtained a higher f_K for cluster galaxies than for field and group ones.

We conclude that a more complete study, extending to more dense environments, is needed to better understand the effect of the environment on the galaxy kinematics.

5. Conclusions

We have presented our new survey HR-COSMOS aimed to obtain the first statistical and representative sample to study the kinematics of star-forming galaxies in the COSMOS field at intermediate redshift. The COSMOS field is a unique treasury of multi-wavelength photometric information, morphological and spectroscopic parameters highly optimized for the study of galaxy evolution and environments in the early Universe. We collected a large sample (766 galaxies) of morphologically blind galaxies at $0 < z < 1.2$, observed with the multi-slit spectrograph ESO-VLT/VIMOS in HR mode. We have aligned each spectral slit along the galaxy major axis, using the information from the high spatial resolution HST/ACS *F814W* imaging data. In this paper, we focused our analysis on the galaxies in the highest redshift range, $0.75 < z < 1.2$. We estimated stellar masses making use of the latest COSMOS photometric catalog (Laigle et al. 2016) derived from the deep-ground and space-based imaging in 30 broad, intermediate, and narrow bands, including the latest data releases from UltraVISTA and *Spitzer*. We modeled the rotation velocity of the galaxies taking into account the instrumental contribution to the observations, such as the seeing and the wavelength resolution. We obtained the rotation velocity at the characteristic radius $R_{2.2}$ to constrain the stellar mass Tully-Fisher relation at $z \sim 0.9$. Our main results are summarized below.

- We obtained velocity rotation measurements of 82 galaxies at $z \simeq 0.9$, of which 80% being rotation-dominated and 20% dispersion-dominated. For the rotation-dominated galaxies, thanks to the relatively large number of galaxies in our sample, we were able to fit the smTF relation without the necessity to set the slope to a local relation, as has often been done in previous works.
- Our smTF best-fit parameters (slope $= 3.68 \pm 0.79$, y-intercept $= 2.15 \pm 0.15$) are formally consistent with previous works in a similar redshift range, like Miller et al. (2011) with spectra obtained with the spectrograph *Keck*/DEIMOS in the GOODS fields and Di Teodoro et al. (2016), who use 3D spectra of a small selected sample of galaxies from ESO-VLT/KMOS. However, our results largely differ from Tiley et al. (2016), who constrained the smTF relation for a sample of rotation-dominated galaxies ($V_{80}/\sigma > 3$) from the KROSS survey.
- No apparent evolution of the smTF relation with redshift was detected when comparing our relation to previous works at lower redshift, such as Pizagno et al. (2005) at $z = 0$ and Puech et al. (2008) at $z \sim 0.6$. We also fitted the smTF relation setting the slope to the $z = 0$ relation form Pizagno et al. (2005) and we found an offset of $\Delta M_* = -0.1$ dex that is within 1σ error on the y-intercept and consistent with no significant evolution predictions from cosmological simulations (Portinari & Sommer-Larsen 2007). Nevertheless, since the sample selection and the details of how the analysis is actually carried out have a strong effect on the results, we will extend our kinematic study to the full sample over $0 < z < 1.2$ to investigate, in a consistent manner, any possible evolution of the smTF relation with redshift.
- The scatter around our smTF relation is smaller than the one obtained by Puech et al. (2008) at $z \sim 0.6$, and larger than the scatter obtained by Pizagno et al. (2005) at $z = 0$ and Miller et al. (2011) at $z \sim 0.9$. We argue that the sample selection plays an important role in the determination of the scatter around the smTF relation, and therefore an internal comparison of the scatter within our own full sample at $0 < z < 1.2$ will be presented in a future work.
- We presented our dynamical mass measurements within the radius $R_{2.2}$ for both rotation- and dispersion-dominated galaxies. To account for the fact that some galaxies are not dynamically supported by the rotation, we introduced an "asymmetric drift correction" term (Meurer et al. 1996), which adds a pressure contribution to the dynamical mass. In comparing the dynamical and stellar masses within $R_{2.2}$ at $z \simeq 0.9$, we find a median stellar-to-dynamical mass ratio equal to 0.20 (for a Chabrier IMF), which means that gas+dark matter masses contribute for 80% of the total mass. Our result is consistent with the stellar-to-dynamical mass fraction measured by Stott et al. (2016) within $R_{2.2}$ for star-forming galaxies from the KROSS survey at $z = 0.8-1.0$, and by Miller et al. (2011) within $R_{2.2}$ across their full sample at $0.2 < z < 1.3$.
- We finally presented our investigation of the dependence of the smTF relation with the environment at $z > 0$, for the first time using the local surface density measurement by

Scoville et al. (2013), obtained with the 2D Voronoi tessellation technique. We have set lower density and higher density environments for the our sample (dispersion-dominated galaxies included) and we computed the scatter around the relation for galaxies in the two environmental bins. We find no dependence of the scatter on environment. We explored whether any effect of the environment exists in constraining the smTF relation and we again fitted the relation, separately, for rotation-dominated galaxies in low- and high-density environments. Still we found no significant offset of the relation consistent with no environmental effect. We note that our sample does not probe the extremes of the COSMOS local density distribution, hence our galaxies in the high-density environmental bin are most likely sitting in a group scale environment. We argue that the gravitational potential created by a group scale environment is possibly not strong enough to kinematically perturb the gas in galaxies. Extending this kinematic study to galaxies in denser environment (cluster-like), is needed to better explore the effect of the environment on the kinematics.

Our analysis demonstrates the power of systematic multi-slit spectroscopy over deep redshift surveys in treasury fields like COSMOS. Even though recent integral field spectroscopy combined with adaptive optics (AO) facilities enable us to retrieve precise 3D velocity map of galaxies, these facilities remain limited in terms of galaxy selection and they require huge amount of telescope time to acquire large representative samples. Multi-slit spectroscopy remains a good complementary alternative to study kinematics of galaxies over deep cosmological fields allowing us to observe, in the case of VIMOS, ~120 galaxies per exposure in a wide field of view, $4\times 7'\times 8'$, much larger than the $\sim 2'\times 2'$ and $1'\times 1'$ fields of view provided by the last generation of IFUs as KMOS and MUSE, respectively.

Acknowledgements. We wish to thank the ESO staff at Paranal Observatory and especially the VIMOS team at ESO for their support during observations. We thank Bodo Ziegler for useful discussion, comments, and suggestions during the preparation of the observations and Katarina Kovač for kindly providing us with their environment measurements. D.P. and L.T. wish to thank Alisson Michel and Bruno Ribeiro for their help with programming codes. We thank Marco Scodeggio for his assistance during the preparation of the observations and the data reduction. D.P. gratefully acknowledges Lori Lubin and UC Davis hospitality during the last phases of the project. We thank Alfred Tiley for providing us with their non-public measurements. This paper is based on data products from observations made with ESO Telescopes at the La Silla Paranal Observatory under ESO programme ID 179.A-2005 and on data products produced by TERAPIX and the Cambridge Astronomy Survey Unit on behalf of the UltraVISTA consortium.

References

Abraham, R. G., van den Bergh, S., & Nair, P. 2003, ApJ, 588, 218
Amram, P., Sullivan, III, W. T., Balkowski, C., Marcelin, M., & Cayatte, V. 1993, ApJ, 403, L59
Arnouts, S., Moscardini, L., Vanzella, E., et al. 2002, MNRAS, 329, 355
Arnouts, S., Le Floc'h, E., Chevallard, J., et al. 2013, A&A, 558, A67
Bacon, R., Brinchmann, J., Richard, J., et al. 2015, A&A, 575, A75
Baldry, I. K., Glazebrook, K., Brinkmann, J., et al. 2004, ApJ, 600, 681
Baldry, I. K., Balogh, M. L., Bower, R. G., et al. 2006, MNRAS, 373, 469
Bamford, S. P., Milvang-Jensen, B., Aragón-Salamanca, A., & Simard, L. 2005, MNRAS, 361, 109
Bamford, S. P., Nichol, R. C., Baldry, I. K., et al. 2009, MNRAS, 393, 1324
Begeman, K. G. 1987, Ph.D. Thesis, Kapteyn Institute, University of Groningen, The Netherlands
Bell, E. F., & de Jong, R. S. 2001, ApJ, 550, 212
Bell, E. F., McIntosh, D. H., Katz, N., & Weinberg, M. D. 2003, ApJS, 149, 289
Blanton, M. R., Hogg, D. W., Bahcall, N. A., et al. 2003, ApJ, 594, 186
Bösch, B., Böhm, A., Wolf, C., et al. 2013, A&A, 554, A97
Bottini, D., Garilli, B., Maccagni, D., et al. 2005, PASP, 117, 996
Brusa, M., Civano, F., Comastri, A., et al. 2010, ApJ, 716, 348
Bruzual, G., & Charlot, S. 2003, MNRAS, 344, 1000
Calzetti, D., Armus, L., Bohlin, R. C., et al. 2000, ApJ, 533, 682
Capak, P., Abraham, R. G., Ellis, R. S., et al. 2007, ApJS, 172, 284
Chabrier, G. 2003, ApJ, 586, L133
Conselice, C. J., Chapman, S. C., & Windhorst, R. A. 2003, ApJ, 596, L5
Conselice, C. J., Bundy, K., Ellis, R. S., et al. 2005, ApJ, 628, 160
Contini, T., Garilli, B., Le Fèvre, O., et al. 2012, A&A, 539, A91
Contini, T., Epinat, B., Bouché, N., et al. 2016, A&A, 591, A49
Cooper, M. C., Newman, J. A., Coil, A. L., et al. 2007, MNRAS, 376, 1445
Coppin, K. E. K., Geach, J. E., Webb, T. M. A., et al. 2012, ApJ, 749, L43
Cortese, L. 2012, A&A, 543, A132
Courteau, S. 1997, AJ, 114, 2402
Courteau, S., Dutton, A. A., van den Bosch, F. C., et al. 2007, ApJ, 671, 203
Dalcanton, J. J., Spergel, D. N., & Summers, F. J. 1997, ApJ, 482, 659
Darvish, B., Sobral, D., Mobasher, B., et al. 2014, ApJ, 796, 51
Darvish, B., Mobasher, B., Sobral, D., Scoville, N., & Aragon-Calvo, M. 2015, ApJ, 805, 121
Di Teodoro, E. M., Fraternali, F., & Miller, S. H. 2016, A&A, 594, A77
Ebeling, H., & Wiedenmann, G. 1993, Phys. Rev. E, 47, 704
Eisenhauer, F., Abuter, R., Bickert, K., et al. 2003, Proc. SPIE, 4841, 1548
Elbaz, D., Daddi, E., Le Borgne, D., et al. 2007, A&A, 468, 33
Epinat, B., Amram, P., Marcelin, M., et al. 2008, MNRAS, 388, 500
Epinat, B., Contini, T., Le Fèvre, O., et al. 2009, A&A, 504, 789
Epinat, B., Amram, P., Balkowski, C., & Marcelin, M. 2010, MNRAS, 401, 2113
Faber, S. M., Phillips, A. C., Kibrick, R. I., et al. 2003, Proc. SPIE, 4841, 1657
Fadda, D., Biviano, A., Marleau, F. R., Storrie-Lombardi, L. J., & Durret, F. 2008, ApJ, 672, L9
Förster Schreiber, N. M., Genzel, R., Bouché, N., et al. 2009, ApJ, 706, 1364
Fraternali, F., & Binney, J. J. 2006, MNRAS, 366, 449
Freeman, K. C. 1970, ApJ, 160, 811
George, M. R., Leauthaud, A., Bundy, K., et al. 2011, ApJ, 742, 125
Glazebrook, K. 2013, PASA, 30, e056
Glazebrook, K., Ellis, R., Santiago, B., & Griffiths, R. 1995, MNRAS, 275, L19
Hammer, F., Flores, H., Puech, M., et al. 2009, A&A, 507, 1313
Haynes, M. P., & Giovanelli, R. 1984, AJ, 89, 758
Hickson, P. 1982, ApJ, 255, 382
Hickson, P. 1993, Astrophys. Lett. Comm., 29, 1
Holmberg, E. 1958, Meddelanden fran Lunds Astronomiska Observatorium Serie II, 136, 1
Ilbert, O., Arnouts, S., McCracken, H. J., et al. 2006, A&A, 457, 841
Ilbert, O., Capak, P., Salvato, M., et al. 2009, ApJ, 690, 1236
Ilbert, O., McCracken, H. J., Le Fèvre, O., et al. 2013, A&A, 556, A55
Ilbert, O., Arnouts, S., Le Floc'h, E., et al. 2015, A&A, 579, A2
Jaffé, Y. L., Aragón-Salamanca, A., Kuntschner, H., et al. 2011, MNRAS, 417, 1996
Kannappan, S. J., Fabricant, D. G., & Franx, M. 2002, AJ, 123, 2358
Kassin, S. A., Weiner, B. J., Faber, S. M., et al. 2007, ApJ, 660, L35
Kassin, S. A., Weiner, B. J., Faber, S. M., et al. 2012, ApJ, 758, 106
Knobel, C., Lilly, S. J., Iovino, A., et al. 2012, ApJ, 753, 121
Kroupa, P. 2001, MNRAS, 322, 231
Laigle, C., McCracken, H. J., Ilbert, O., et al. 2016, ApJS, 224, 24
Le Fèvre, O., Saisse, M., Mancini, D., et al. 2003, Proc. SPIE, 4841, 1670
Lee, N., Sanders, D. B., Casey, C. M., et al. 2015, ApJ, 801, 80
Lemaux, B. C., Le Floc'h, E., Le Fèvre, O., et al. 2014, A&A, 572, A90
Lilly, S. J., Le Fèvre, O., Renzini, A., et al. 2007, ApJS, 172, 70
Lotz, J. M., Primack, J., & Madau, P. 2004, AJ, 128, 163
Markwardt, C. B. 2009, in Astronomical Data Analysis Software and Systems XVIII, ASP Conf. Ser., 411, 251
Masters, K. L., Mosleh, M., Romer, A. K., et al. 2010, MNRAS, 405, 783
McCracken, H. J., Milvang-Jensen, B., Dunlop, J., et al. 2012, A&A, 544, A156
McGaugh, S. S. 2005, ApJ, 632, 859
Meurer, G. R., Carignan, C., Beaulieu, S. F., & Freeman, K. C. 1996, AJ, 111, 1551
Miller, S. H., Bundy, K., Sullivan, M., Ellis, R. S., & Treu, T. 2011, ApJ, 741, 115
Mocz, P., Green, A., Malacari, M., & Glazebrook, K. 2012, MNRAS, 425, 296
Moran, S. M., Miller, N., Treu, T., Ellis, R. S., & Smith, G. P. 2007, ApJ, 659, 1138
Nakamura, O., Aragón-Salamanca, A., Milvang-Jensen, B., et al. 2006, MNRAS, 366, 144
Newman, J. A., Cooper, M. C., Davis, M., et al. 2013a, ApJS, 208, 5
Newman, S. F., Genzel, R., Förster Schreiber, N. M., et al. 2013b, ApJ, 767, 104
Osterbrock, D. E. 1989, Astrophysics of gaseous nebulae and active galactic nuclei (University Science Books)
Pizagno, J., Prada, F., Weinberg, D. H., et al. 2005, ApJ, 633, 844

Pizagno, J., Prada, F., Weinberg, D. H., et al. 2007, AJ, 134, 945
Porter, S. C., Raychaudhury, S., Pimbblet, K. A., & Drinkwater, M. J. 2008, MNRAS, 388, 1152
Portinari, L., & Sommer-Larsen, J. 2007, MNRAS, 375, 913
Postman, M., Franx, M., Cross, N. J. G., et al. 2005, ApJ, 623, 721
Puech, M., Flores, H., Hammer, F., et al. 2008, A&A, 484, 173
Puech, M., Hammer, F., Flores, H., et al. 2010, A&A, 510, A68
Puech, M., Hammer, F., Hopkins, P. F., et al. 2012, ApJ, 753, 128
Reyes, R., Mandelbaum, R., Gunn, J. E., Pizagno, J., & Lackner, C. N. 2011, MNRAS, 417, 2347
Salpeter, E. E. 1955, ApJ, 121, 161
Sargent, M. T., Carollo, C. M., Lilly, S. J., et al. 2007, ApJS, 172, 434
Scarlata, C., Carollo, C. M., Lilly, S., et al. 2007, ApJS, 172, 406
Scodeggio, M., Franzetti, P., Garilli, B., et al. 2005, PASP, 117, 1284
Scoville, N. Z., Young, J. S., & Lucy, L. B. 1983, ApJ, 270, 443
Scoville, N., Aussel, H., Brusa, M., et al. 2007, ApJS, 172, 1
Scoville, N., Arnouts, S., Aussel, H., et al. 2013, ApJS, 206, 3
Sharples, R., Bender, R., Agudo Berbel, A., et al. 2013, The Messenger, 151, 21
Simard, L., Willmer, C. N. A., Vogt, N. P., et al. 2002, ApJS, 142, 1
Simons, R. C., Kassin, S. A., Weiner, B. J., et al. 2015, MNRAS, 452, 986
Sobral, D., Best, P. N., Smail, I., et al. 2011, MNRAS, 411, 675
Sommer-Larsen, J., Götz, M., & Portinari, L. 2003, ApJ, 596, 47
Steinhardt, C. L., Speagle, J. S., Capak, P., et al. 2014, ApJ, 791, L25
Stott, J. P., Swinbank, A. M., Johnson, H. L., et al. 2016, MNRAS, 457, 1888
Tiley, A. L., Stott, J. P., Swinbank, A. M., et al. 2016, MNRAS, 460, 103
Torres-Flores, S., Mendes de Oliveira, C., Amram, P., et al. 2010, A&A, 521, A59
Torres-Flores, S., Mendes de Oliveira, C., Plana, H., Amram, P., & Epinat, B. 2013, MNRAS, 432, 3085
Torres-Flores, S., Amram, P., Mendes de Oliveira, C., et al. 2014, MNRAS, 442, 2188
Tran, K.-V. H., Saintonge, A., Moustakas, J., et al. 2009, ApJ, 705, 809
Tremaine, S., Gebhardt, K., Bender, R., et al. 2002, ApJ, 574, 740
Tully, R. B., & Fisher, J. R. 1977, A&A, 54, 661
Verheijen, M. A. W. 1997, Ph.D. Thesis, Univ. Groningen, The Netherlands
Verheijen, M. A. W. 2001, ApJ, 563, 694
Weiner, B. J., Willmer, C. N. A., Faber, S. M., et al. 2006a, ApJ, 653, 1049
Weiner, B. J., Willmer, C. N. A., Faber, S. M., et al. 2006b, ApJ, 653, 1027
Williams, M. J., Bureau, M., & Cappellari, M. 2010, MNRAS, 409, 1330
Willick, J. A. 1994, ApJS, 92, 1
Wisnioski, E., Förster Schreiber, N. M., Wuyts, S., et al. 2015, ApJ, 799, 209
Wuyts, S., Förster Schreiber, N. M., Genzel, R., et al. 2012, ApJ, 753, 114
Wuyts, S., Förster Schreiber, N. M., Nelson, E. J., et al. 2013, ApJ, 779, 135
Wuyts, S., Förster Schreiber, N. M., Wisnioski, E., et al. 2016, A&A, 831, 149
Zafar, T., Péroux, C., Popping, A., et al. 2013, A&A, 556, A141
Ziegler, B. L., Böhm, A., Jäger, K., Heidt, J., & Möllenhoff, C. 2003, ApJ, 598, L87

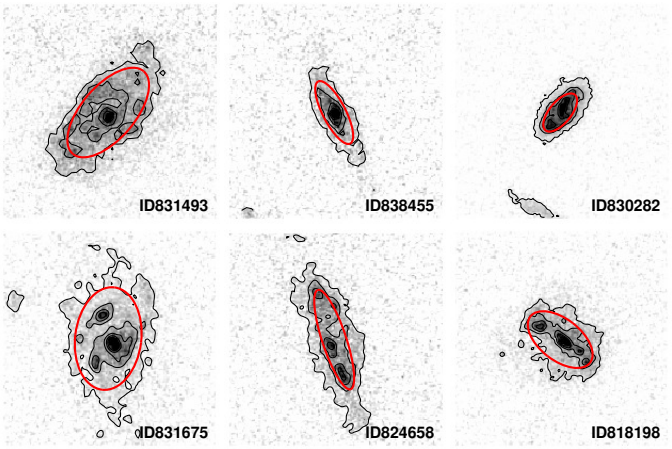

Fig. A.1. Example of the visual check of the correctness of the inclination adopted in our kinematic analysis, by placing ellipses (in red) with the axial ratio b/a from the Zurich Structure and Morphology Catalog on HST/ACS *F814W* galaxy images. The contours begin at 1σ and continue with 2σ step.

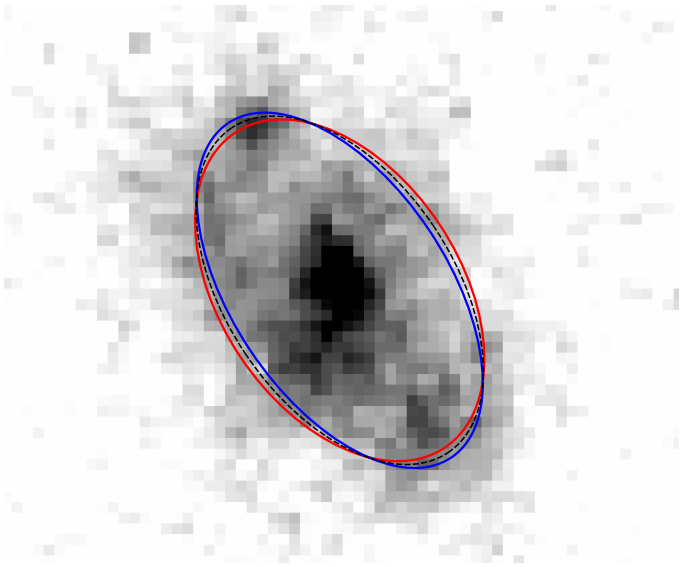

Fig. A.2. Example of the ellipse that overlaps the HST/ACS image with b/a as measured in the Zurich Structure and Morphology Catalog (black dashed ellipse) and as it appears using the lower (red solid ellipse) and upper (blue solid ellipse) value of b/a measured in Eq. (A.1).

Appendix A: Uncertainties on the axial ratio *b/a*

The adopted b/a is included in the Zurich Structure and Morphology Catalog and was measured with a software (GIM2D, see Sect. 2.1) that gives morphological measurements corrected for the instrumental PSF. We used the axial ratio to derive the inclination of the galaxies of our sub-sample at $z \sim 0.9$.

The inclination is an important parameter in our kinematic analysis since it scales the observed velocity to obtain the galaxy intrinsic velocity rotation (see Eq. (3)). Therefore, we visually checked the correctness of this parameter by overlapping an ellipse with the adopted b/a on the HST/ACS *F814W* image of each galaxy. We plot this visualization for a randomly chosen subset of six galaxies drawn from our main sample in Fig. A.1. Since the GIM2D measurements in the catalog only included the value of the ellipticity $(1 - b/a)$, but not those of a and b, we adopted as major axis a quantity called $r80$ from the Zurich Structure and Morphology Catalog. This quantity is defined as the semi-major axis length of an ellipse encompassing 80% of total light, with the adopted minor axis being, therefore, equal to $r80$ scaled by b/a. This inspection allowed us to ensure that the inclinations employed in our kinematic analysis are reasonably measured and that they do not bias the rotation velocity derived.

However, systematic uncertainties on the axial ratio measurements due to small variations of the instrument PSF must be taken into account in the velocity error budget. To that end, following (Epinat et al. 2009), we estimated upper and lower limits for the axial ratio b/a. As before, we adopted $a = r_{80}$ and $b = r_{80} \times b/a$. We obtain that b/a, as a result of the small variation of the PSF, which we assume to be the same for both major and minor axes and equal to one third of the HST/ACS PSF (where the ACS PSF is $\sim 0.1''$), can vary in the following range:

$$\frac{b-\Delta}{a+\Delta} \leq \frac{b}{a} \leq \frac{b+\Delta}{a-\Delta} \tag{A.1}$$

with $\Delta = 0.03$. In Fig. A.2, we show an example of how the ellipse overlapped to the HST/ACS image changes when using the upper and lower limit of the axial ratio.

We quantified that the relative uncertainties coming from the small variations of the instrument PSF go from a minimum of 6% to a maximum of 30%. These uncertainties are propagated to the inclination and the rotation velocity, the values of which are presented in Table E.1.

Appendix B: Model of the galaxy surface brightness

We showed in Sect. 4 that our models are not always able to reproduce the observed spectra light profile. These models are particularly ineffective at high redshift where galaxies are known to exhibit clumpy star formation.

Here we test the effect of our assumption about exponential disc profile on our derived rotation velocities. To that end, we used an algorithm from Scoville et al. (1983; see Sect. 3 therein for a detailed description), which derives the spatial line emission distribution (even non-axisymmetric) at high-resolution that best matches the observed emission line profile. Since the algorithm was not implemented to work with doublet emission lines, we made our test on galaxies with Hα emission line spectra from our sample at lower redshift. For those galaxies we fitted the observed spectrum with kinematic models obtained with both an exponential surface brightness profile and the profile derived by the algorithm. The comparison between the two best-fit models for three cases at redshift $z = 0.0726$, $z = 0.2494$ and $z = 0.1125$ is shown in Fig. B.1.

We find that the models with the light profile derived with the algorithm from Scoville et al. (1983; right panels) reproduce much better the observed emission line than the models obtained with the exponential profile (middle panels). If we compare the rotation velocity $V_{\rm ROT}$ estimated with both models (values given in the upper right corners with their associated uncertainties), we find that they are always consistent within the uncertainties. We claim, therefore, that there is no effect from the modeled surface brightness profile in the derivation of the galaxy rotation velocity.

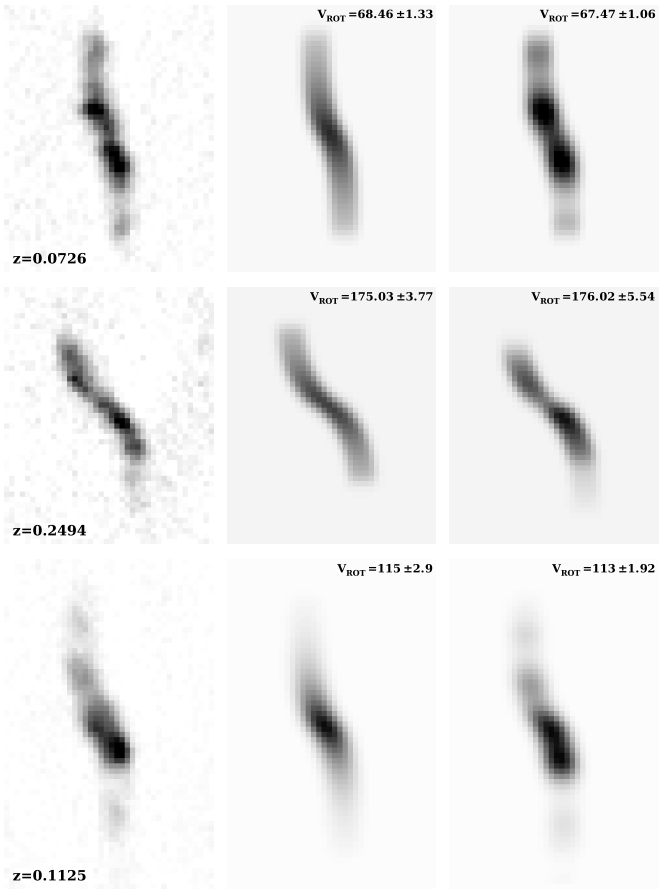

Fig. B.1. Comparison between two modeling techniques for three cases with the Hα emission line observed at $z = 0.0726$, $z = 0.2494$ and $z = 0.1125$. *Left panels*: continuum subtracted 2D spectra centered at Hα. *Middle panels*: best-fit models to the emission line with an exponential disc light profile. *Right panels*: best-fit models to the emission line with the light profile estimated from the algorithm from Scoville et al. (1983). The measurement of the velocity best-fit parameter within its uncertainties is given in the upper right corners. The images scale is: 1 pixel = 0.205″ in the spatial direction and 1 pixel = 0.6 Å in the spectral direction.

Appendix C: [O II] doublet measurements

We provide our measurements of the ratio $R_{[OII]}$, the rest-frame EW, and the SFR derived from both SED-fitting and the [OII] EW. They are listed in Table E.2. The value of $R_{[OII]}$ was computed during our modeling of the galaxy kinematics (see Sect. 3.2), and is defined as the flux ratio between the line at longer wavelength ($\lambda = 3729$ Å) and the one at shorter wavelength ($\lambda = 3726$ Å). Figure C.1 shows $R_{[OII]}$ distribution for our sample at $0.75 < z < 1.2$. It is consistent with the range of values computed by Osterbrock (1989), from $R_{[OII]} = 0.35$ in the limit of high electronic density ($N_e \to \infty$) to $R_{[OII]} = 1.5$ in the limit of low electronic density ($N_e \to 0$) for temperatures typical of star-forming regions ($T \sim 10^4 K$).

Figure C.2 present $R_{[OII]}$ versus the velocity dispersion (top panel), the stellar mass (middle panel) and the SFR_{SED} (bottom panel). We find that the electronic density (probed by $R_{[OII]}$) for those star-forming disc galaxies does not depend on the velocity dispersion (both for dispersion- and rotation-dominated galaxies), nor on the stellar mass or the star formation rate.

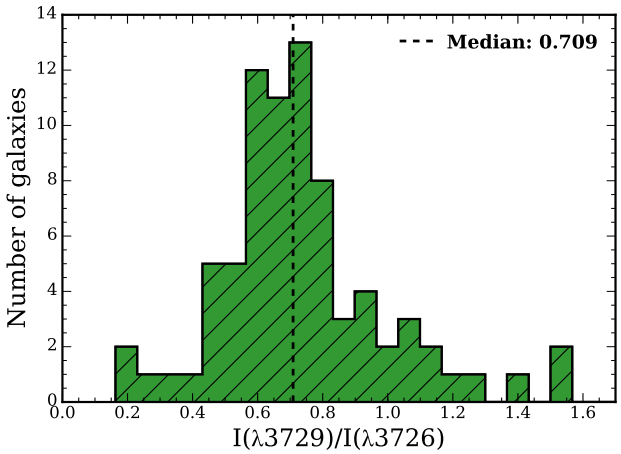

Fig. C.1. Intensity ratio of the [OII] doublet distribution of our galaxy sample at $z \simeq 0.9$. The vertical dotted line lies at the median value of the distribution.

We note that the spread of the electronic density values appears larger in massive galaxies ($M_* > 10^{10} M_\odot$).

The EW([OII]) is computed by defining two "continuum" bandpasses, slightly blueward and redward of the [OII] doublet, which are used to estimate the stellar continuum across the spectral feature. An additional "feature" bandpass is defined to include the spectral line. The stellar continuum is computed as the median value over the two continuum bandpasses. The bandpasses were chosen by eye for each galaxy spectrum to avoid possible contaminating features near the spectral lines of interest. The EW is defined as

$$EW(\text{Å}) = \sum_{i=0}^{n} \frac{C_i - F_i}{C_i} \Delta\lambda_i, \tag{C.1}$$

where F_i is the flux in the ith spectral pixel in the feature bandpass, C_i is the continuum flux in the ith spectral pixel over the same bandpass, and $\Delta\lambda_i$ is the pixel scale of the spectrum (Å/pixel). Errors in the EW were derived using the Poisson errors on the spectral feature. Given this definition of EW, the convention adopted in this work is for negative EWs to correspond to spectral lines observed in emission. The SFR_{SED} is computed making use of the Le Phare software (Arnouts et al. 2002; Ilbert et al. 2006) following the same recipes applied to compute the stellar masses (Sect. 2.4). The $SFR_{[OII]}$ is computed using the equation (5) from Lemaux et al. (2014) based on SFR formula of Kewley et al. (2004) and adapted to substitute the [OII] flux with the measurement of EW([OII]). The choice of using EW([OII]) instead of [OII] flux was motivated by the lack of the absolute flux calibration for our spectroscopic observations (see Sect. 2.3). We show the relation between the computed $SFR_{[OII]}$ uncorrected for the internal extinction and the EW([OII] in Fig. C.3. The correction for the internal extinction was applied using a prescription proposed by Wuyts et al. (2013), based on the stellar continuum reddening from the SED fitting, modified to take into account an extra extinction expected from the HII regions.

In Fig. C.4, we show the comparison between the $SFR_{[OII]}$ and SFR_{SED}. Our two SFR estimations are in a very good agreement.

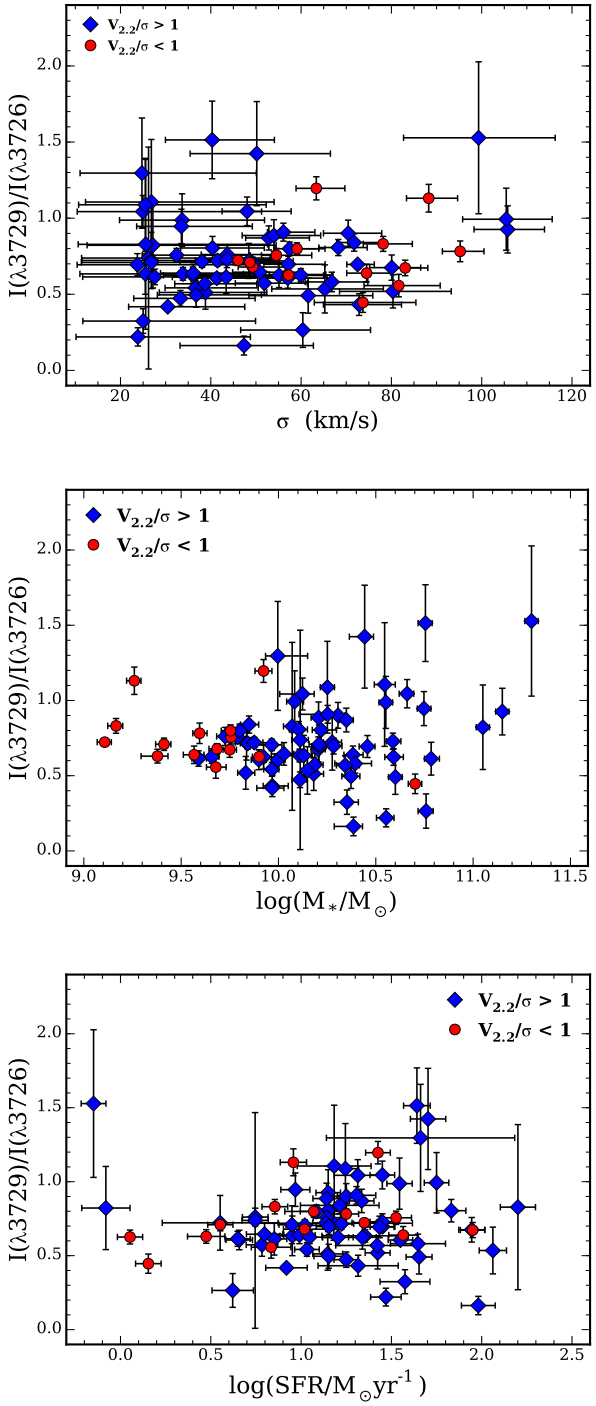

Fig. C.2. Intensity ratio of the [OII] doublet versus velocity dispersion (*top*), stellar mass (*middle*) and SFR_{SED} (*bottom*). The blue diamonds and the red circles show the rotation- and dispersion-dominated galaxies, respectively.

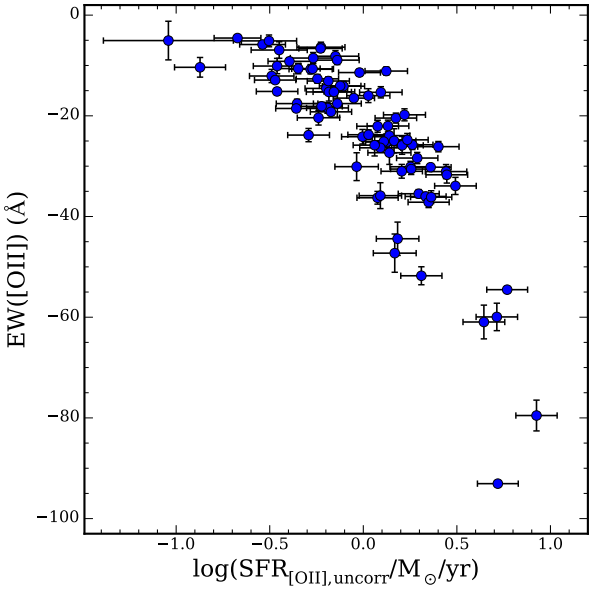

Fig. C.3. [OII] equivalent width versus log SFR computed from [OII] emission line and uncorrected for interstellar extinction.

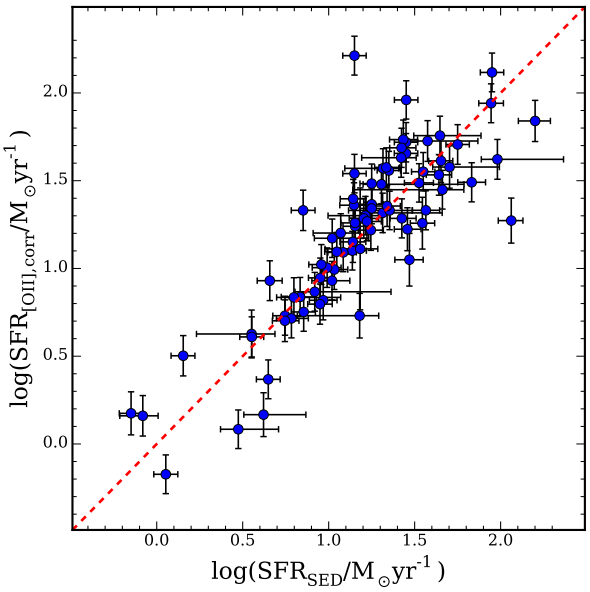

Fig. C.4. Comparison of SFR computed from SED fitting process and [OII] emission line corrected for internal extinction in logarithmic units. The red dashed line represents the 1:1 relation.

Appendix D: Scatter around the smTF relation

Physical scatter around the smTF relation can be due to variations in the stellar mass fraction (stellar-to-total mass ratio), or differences in how the observed rotation velocity relates to the total mass (Kannappan et al. 2002), or a combination of the two. We decided, therefore, to geometrically compute the scatter around the smTF relation as the shortest distance d_w of the data from the relation weighted by the uncertainties, since d_w carries information on the physical scatter coming from both the stellar mass and the rotation velocity. We used this approach in our investigation of the dependence of the smTF relation with the environment (Sect. 4.4). In Fig. D.1 we show the distances computed from our smTF relation, color coded according to our environment definition (purple squares for higher density and pink diamonds for lower density environment). In the upper left corner of the plot we show a scheme of the geometry used to compute the scatter. Following the trigonometry, we defined the distance d between the data point $P(x, y)$ and the point $P_{\rm fit}(x_{\rm fit}, y_{\rm fit})$

on the relation as

$$d = \frac{|\, r_1 \, \sin\theta \,| + |\, r_2 \, \cos\theta \,|}{2}, \tag{D.1}$$

where θ is the angle between the relation and the positive direction of the x-axis, and is expressed as $\theta = \arctan(slope)$, and r_1 (or r_2) is the distance between the x value (or the y value) of the data points and the relation at fixed value of y (or x). We chose to define d as in Eq. (D.1), so that we can include the uncertainties from both the x and y variables in the error budget. Therefore the scatter error is expressed as

$$\delta_{\rm d} = \frac{\sqrt{(\delta_{\rm r_1} \, \sin\theta)^2 + (\delta_{\rm r_2} \, \cos\theta)^2}}{2}. \tag{D.2}$$

We then computed the weighted d_w as

$$d_w = d/\delta_{\rm d}. \tag{D.3}$$

In Sect. 4.2, we did not use this approach to compute the intrinsic scatter $\sigma_{\rm intr}$ of the rotation-dominated galaxy sample around the smTR relation to ease the comparison of our results with previous works. In the study of possible dependencies of the smTF relation with the environment, instead, we made a comparison internal to our sample between scatters for galaxies in two different environments, and the distance d_w was a more appropriate quantity for this purpose.

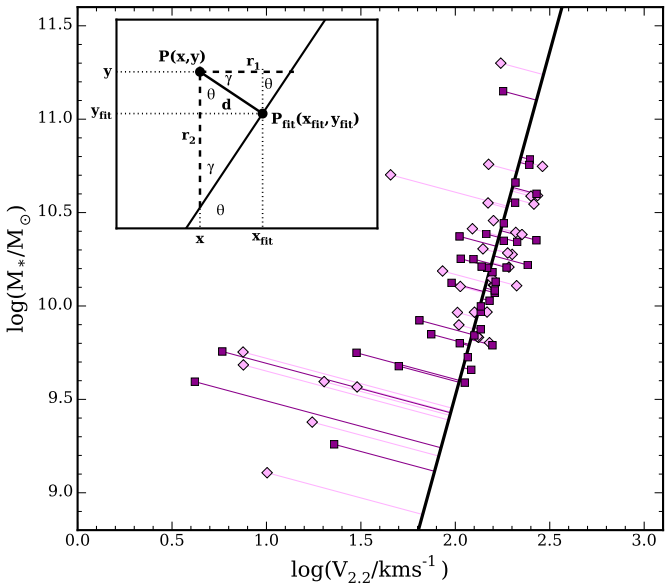

Fig. D.1. Distances d_w of the data points from the smTF relation. Pink diamonds and purple squares with relative lines refer to galaxies in lower and higher density environment, respectively. The *embedded plot* in the upper left corner show a simplified scheme of the geometry used to compute d_w (see text Appendix D).

Appendix E: Additional tables

Table E.1. Galaxy parameters.

ID	RA	Dec	z	PA	INCL	$R_{2.2}$	$V_{2.2}$	σ	$V_{2.2}/\sigma$	$\log(M_*/M_\odot)$	$\log(M_{\rm dyn}(R_{2.2})/M_\odot)$
	deg	deg		deg	deg	kpc	km s^{-1}	km s^{-1}			
(1)	(2)	(3)	(4)	(5)	(6)	(7)	(8)	(9)	(10)	(11)	(12)
824384	150.200439	2.218330	0.8795	$-29.0^{+1.2}_{-1.2}$	$52.7^{+7.6}_{-6.8}$	3.7	249^{+32}_{-30}	43^{+15}_{-12}	$5.7^{+2.1}_{-1.7}$	$10.78^{+0.04}_{-0.03}$	$10.76^{+0.11}_{-0.10}$
824508	150.173050	2.157201	0.8931	$+45.1^{+0.6}_{-0.6}$	$62.8^{+2.6}_{-2.5}$	17.7	273^{+22}_{-21}	36^{+13}_{-7}	$7.6^{+2.7}_{-1.5}$	$10.59^{+0.05}_{-0.04}$	$11.50^{+0.07}_{-0.07}$
824658	150.142609	2.197006	0.8535	$+18.3^{+0.4}_{-0.3}$	$78.3^{+2.8}_{-2.7}$	10.2	208^{+8}_{-8}	48^{+10}_{-6}	$4.3^{+0.9}_{-0.5}$	$10.66^{+0.03}_{-0.04}$	$11.06^{+0.03}_{-0.03}$
824791	150.110275	2.138679	0.8377	$+6.4^{+1.5}_{-1.7}$	$49.1^{+8.2}_{-7.3}$	4.7	159^{+20}_{-18}	26^{+27}_{-15}	$6.1^{+6.3}_{-3.5}$	$10.11^{+0.04}_{-0.04}$	$10.46^{+0.11}_{-0.10}$
824847	150.097351	2.146748	0.9364	$-33.8^{+1.3}_{-1.0}$	$64.3^{+4.4}_{-4.1}$	7.7	181^{+21}_{-21}	50^{+16}_{-15}	$3.6^{+1.2}_{-1.1}$	$10.44^{+0.05}_{-0.08}$	$10.83^{+0.09}_{-0.09}$
824675	150.137985	2.281988	0.8939	$-41.3^{+1.6}_{-2.0}$	$62.1^{+6.1}_{-5.5}$	8.8	86^{+12}_{-12}	52^{+10}_{-6}	$1.7^{+0.4}_{-0.3}$	$10.19^{+0.04}_{-0.04}$	$10.43^{+0.10}_{-0.08}$
831229	150.200668	2.375840	0.7962	$-53.4^{+2.1}_{-2.4}$	$41.4^{+8.0}_{-7.3}$	5.6	200^{+33}_{-31}	27^{+28}_{-15}	$7.5^{+7.9}_{-4.4}$	$10.28^{+0.05}_{-0.04}$	$10.73^{+0.14}_{-0.13}$
831256	150.194794	2.311815	0.8926	$-6.2^{+0.6}_{-0.8}$	$72.9^{+2.8}_{-2.6}$	10.6	209^{+12}_{-11}	67^{+8}_{-6}	$3.1^{+0.4}_{-0.3}$	$10.39^{+0.08}_{-0.10}$	$11.12^{+0.04}_{-0.04}$
831534	150.136124	2.370541	0.9267	$-34.8^{+0.8}_{-0.7}$	$52.1^{+4.1}_{-3.9}$	7.6	174^{+27}_{-27}	99^{+17}_{-17}	$1.8^{+0.4}_{-0.4}$	$11.30^{+0.03}_{-0.03}$	$10.96^{+0.10}_{-0.10}$
831675	150.107437	2.329219	0.9236	$-6.8^{+1.0}_{-0.8}$	$50.5^{+3.9}_{-3.7}$	11.7	246^{+40}_{-40}	40^{+14}_{-10}	$6.1^{+2.3}_{-1.9}$	$10.75^{+0.03}_{-0.04}$	$11.24^{+0.13}_{-0.13}$
701002	149.998444	2.289785	0.9783	$+41.2^{+0.6}_{-0.6}$	$67.2^{+4.7}_{-4.2}$	5.1	157^{+17}_{-17}	39^{+14}_{-10}	$4.1^{+1.5}_{-1.2}$	$10.18^{+0.05}_{-0.05}$	$10.52^{+0.09}_{-0.09}$
832385	149.987930	2.364365	0.9301	$+2.2^{+0.8}_{-0.9}$	$69.7^{+3.4}_{-3.2}$	10.2	269^{+12}_{-12}	25^{+25}_{-13}	$10.7^{+10.7}_{-5.8}$	$10.35^{+0.06}_{-0.07}$	$11.24^{+0.04}_{-0.04}$
825474	149.982162	2.177024	0.8818	$+37.8^{+1.7}_{-1.9}$	$44.9^{+6.1}_{-5.6}$	9.2	289^{+34}_{-32}	33^{+16}_{-10}	$8.6^{+4.2}_{-2.7}$	$10.75^{+0.04}_{-0.03}$	$11.27^{+0.10}_{-0.09}$
823045	150.478516	2.163036	0.8886	$+36.6^{+0.3}_{-0.3}$	$73.6^{+2.5}_{-2.4}$	9.4	163^{+7}_{-7}	25^{+26}_{-14}	$6.4^{+6.7}_{-3.7}$	$10.13^{+0.04}_{-0.04}$	$10.79^{+0.06}_{-0.04}$
823323	150.423203	2.223220	0.8830	$-49.8^{+0.4}_{-0.3}$	$70.5^{+2.3}_{-2.2}$	9.6	162^{+4}_{-4}	26^{+27}_{-15}	$6.3^{+6.7}_{-3.7}$	$10.07^{+0.05}_{-0.04}$	$10.79^{+0.05}_{-0.03}$
829955	150.444427	2.369805	0.8909	$+11.6^{+2.4}_{-3.1}$	$33.4^{+8.8}_{-8.0}$	4.0	156^{+54}_{-52}	65^{+13}_{-12}	$2.4^{+1.0}_{-0.9}$	$10.15^{+0.03}_{-0.03}$	$10.49^{+0.22}_{-0.21}$
824317	150.212723	2.159449	0.9817	$+32.4^{+0.5}_{-0.8}$	$63.2^{+4.4}_{-4.0}$	5.8	65^{+8}_{-8}	55^{+10}_{-8}	$1.2^{+0.3}_{-0.2}$	$9.92^{+0.06}_{-0.05}$	$10.16^{+0.10}_{-0.09}$
827096	149.657990	2.269869	0.8309	$+7.4^{+0.6}_{-0.6}$	$59.4^{+3.5}_{-3.2}$	7.6	181^{+9}_{-9}	53^{+9}_{-5}	$3.4^{+0.6}_{-0.4}$	$10.35^{+0.04}_{-0.03}$	$10.83^{+0.04}_{-0.04}$
833862	149.698212	2.367727	0.7512	$+26.5^{+0.5}_{-0.7}$	$67.9^{+4.1}_{-3.8}$	6.6	133^{+24}_{-24}	80^{+13}_{-12}	$1.7^{+0.4}_{-0.4}$	$9.83^{+0.05}_{-0.04}$	$10.69^{+0.11}_{-0.11}$
834100	149.655685	2.362452	0.8676	$+55.4^{+0.7}_{-0.7}$	$66.4^{+5.4}_{-4.9}$	3.1	23^{+17}_{-17}	88^{+6}_{-5}	$0.3^{+0.2}_{-0.2}$	$9.26^{+0.03}_{-0.04}$	$10.10^{+0.06}_{-0.05}$
826948	149.687210	2.208733	0.9445	$+35.7^{+0.9}_{-0.7}$	$59.6^{+3.6}_{-3.4}$	8.3	147^{+13}_{-13}	80^{+6}_{-5}	$1.8^{+0.2}_{-0.2}$	$10.20^{+0.04}_{-0.04}$	$10.84^{+0.05}_{-0.05}$
827050	149.666428	2.222278	0.8922	$+57.7^{+1.1}_{-0.9}$	$42.8^{+7.4}_{-6.7}$	5.9	179^{+36}_{-34}	106^{+8}_{-7}	$1.7^{+0.4}_{-0.3}$	$11.15^{+0.03}_{-0.03}$	$10.89^{+0.10}_{-0.10}$
837355	150.392242	2.603468	0.8248	$-11.9^{+0.8}_{-0.8}$	$66.3^{+3.8}_{-3.6}$	7.9	29^{+10}_{-10}	49^{+9}_{-4}	$0.6^{+0.2}_{-0.2}$	$9.41^{+0.04}_{-0.04}$	$10.04^{+0.14}_{-0.07}$
838455	150.189224	2.606611	1.0196	$+27.4^{+0.7}_{-0.6}$	$72.0^{+3.8}_{-3.5}$	7.9	207^{+40}_{-40}	24^{+25}_{-14}	$8.7^{+9.2}_{-5.3}$	$10.55^{+0.04}_{-0.05}$	$10.91^{+0.16}_{-0.16}$
831223	150.202377	2.377197	0.7965	$+46.0^{+1.3}_{-1.2}$	$59.2^{+5.4}_{-4.9}$	5.3	261^{+17}_{-15}	27^{+27}_{-15}	$9.7^{+9.9}_{-5.3}$	$10.55^{+0.05}_{-0.05}$	$10.93^{+0.06}_{-0.05}$
1254477	150.003080	2.400714	0.9447	$-6.9^{+1.5}_{-1.7}$	$47.1^{+4.9}_{-4.6}$	10.0	212^{+19}_{-18}	39^{+11}_{-7}	$5.5^{+1.7}_{-1.1}$	$10.34^{+0.07}_{-0.05}$	$11.05^{+0.07}_{-0.07}$
840112	149.907379	2.529695	0.8908	$+38.4^{+3.4}_{-2.5}$	$47.4^{+6.1}_{-5.8}$	6.7	150^{+35}_{-35}	60^{+15}_{-14}	$2.5^{+0.9}_{-0.8}$	$10.76^{+0.04}_{-0.04}$	$10.67^{+0.16}_{-0.16}$
840266	149.878723	2.601216	0.9587	$-32.1^{+1.0}_{-1.3}$	$60.1^{+3.6}_{-3.4}$	8.7	107^{+7}_{-7}	56^{+7}_{-4}	$1.9^{+0.3}_{-0.2}$	$10.25^{+0.06}_{-0.15}$	$10.57^{+0.06}_{-0.04}$
840390	149.851700	2.519398	0.8452	$-24.6^{+0.5}_{-0.4}$	$62.7^{+3.6}_{-3.3}$	6.8	161^{+22}_{-22}	33^{+17}_{-10}	$4.8^{+2.5}_{-1.6}$	$10.11^{+0.03}_{-0.04}$	$10.65^{+0.11}_{-0.11}$
833209	149.826096	2.382653	1.1210	$-23.8^{+0.7}_{-0.7}$	$62.3^{+5.2}_{-4.8}$	4.2	56^{+8}_{-8}	63^{+6}_{-4}	$0.9^{+0.2}_{-0.1}$	$9.92^{+0.04}_{-0.04}$	$10.06^{+0.07}_{-0.06}$
811224	150.282700	1.932057	0.9137	$+8.3^{+7.0}_{-7.1}$	$46.2^{+4.2}_{-3.9}$	13.7	269^{+37}_{-36}	62^{+14}_{-13}	$4.4^{+1.2}_{-1.1}$	$10.60^{+0.04}_{-0.04}$	$11.41^{+0.11}_{-0.11}$
811233	150.280426	1.921645	1.0099	$+33.7^{+0.8}_{-0.8}$	$54.8^{+6.2}_{-5.6}$	5.1	123^{+10}_{-9}	24^{+25}_{-14}	$5.1^{+5.4}_{-3.0}$	$10.41^{+0.04}_{-0.05}$	$10.29^{+0.09}_{-0.07}$
817262	150.373260	2.086616	0.9294	$+24.8^{+0.4}_{-0.4}$	$72.4^{+3.0}_{-2.8}$	7.3	96^{+2}_{-2}	25^{+26}_{-15}	$3.8^{+4.0}_{-2.2}$	$10.12^{+0.06}_{-0.12}$	$10.25^{+0.12}_{-0.07}$
817416	150.343170	2.057282	0.9351	$+55.0^{+0.6}_{-0.6}$	$58.1^{+7.6}_{-6.7}$	3.2	4^{+11}_{-11}	95^{+5}_{-4}	$0.0^{+0.1}_{-0.1}$	$9.59^{+0.04}_{-0.03}$	$10.16^{+0.05}_{-0.04}$
818198	150.176285	2.111890	0.7872	$+52.2^{+0.8}_{-0.6}$	$57.2^{+3.6}_{-3.4}$	8.0	75^{+9}_{-9}	72^{+7}_{-4}	$1.0^{+0.2}_{-0.1}$	$9.85^{+0.05}_{-0.04}$	$10.49^{+0.07}_{-0.05}$
811727	150.176453	1.955227	1.1494	$-42.1^{+1.6}_{-1.6}$	$59.0^{+5.0}_{-4.6}$	6.2	146^{+33}_{-33}	47^{+15}_{-14}	$3.1^{+1.2}_{-1.2}$	$10.39^{+0.05}_{-0.10}$	$10.58^{+0.17}_{-0.17}$

Notes. (1) Source HR-COSMOS identification number; (2) and (3) right ascension and declination J2000 coordinates; (4) HR-COSMOS spectroscopic redshift; (5) morphological galaxy position angle, defined as the angle measured counterclockwise (East of North) between the North direction in the sky and the galaxy major axis, from Zurich Structure and Morphology Catalog (Sargent et al. 2007); (6) inclination, defined as the angle between the line of sight and the normal to the plane of the galaxy (i = 0 for face-on galaxies), from the HST/ACS *F814W* images (Zurich Structure and Morphology Catalog, Sargent et al. 2007); (7) characteristic radius 2.2 times the galaxy disc scale length (Zurich Structure and Morphology Catalog, Scarlata et al. 2007); (8) rotation velocity measured from the kinematic models at $R_{2.2}$; (9) velocity dispersion from the kinematic models; (10) ratio between $V_{2.2}$ and the velocity dispersion σ; (11) log of the stellar mass computed as described in Sect. 2.4; (12) log of the dynamical mass.

Table E.1. continued.

ID	RA	Dec	z	PA	INCL	$R_{2.2}$	$V_{2.2}$	σ	$V_{2.2}/\sigma$	$\log(M_*/M_\odot)$	$\log(M_{\rm dyn}(R_{2.2})/M_\odot)$
	deg	deg		deg	deg	kpc	km s^{-1}	km s^{-1}			
(1)	(2)	(3)	(4)	(5)	(6)	(7)	(8)	(9)	(10)	(11)	(12)
818959	150.017838	2.049238	0.8724	$-59.6^{+1.3}_{-1.7}$	$47.2^{+5.2}_{-4.8}$	7.1	131^{+22}_{-22}	48^{+10}_{-6}	$2.7^{+0.7}_{-0.6}$	$9.84^{+0.13}_{-0.06}$	$10.56^{+0.12}_{-0.12}$
819479	149.890701	2.089932	0.7505	$+20.5^{+1.1}_{-1.3}$	$60.6^{+4.0}_{-3.8}$	7.3	17^{+7}_{-7}	57^{+8}_{-4}	$0.3^{+0.1}_{-0.1}$	$9.38^{+0.05}_{-0.08}$	$10.10^{+0.12}_{-0.06}$
819641	149.852707	2.100561	0.8957	$-49.8^{+1.8}_{-1.8}$	$42.4^{+7.5}_{-6.9}$	5.7	149^{+41}_{-40}	34^{+18}_{-14}	$4.4^{+2.7}_{-2.2}$	$10.55^{+0.03}_{-0.04}$	$10.51^{+0.22}_{-0.21}$
819765	149.819427	2.093724	0.8543	$-1.6^{+0.5}_{-0.5}$	$67.9^{+3.5}_{-3.3}$	6.6	136^{+11}_{-11}	73^{+9}_{-8}	$1.9^{+0.3}_{-0.3}$	$9.97^{+0.08}_{-0.05}$	$10.66^{+0.06}_{-0.06}$
812913	149.912201	1.923351	0.7747	$+43.3^{+0.6}_{-0.6}$	$56.1^{+4.5}_{-4.2}$	6.5	184^{+12}_{-12}	27^{+27}_{-15}	$6.8^{+6.8}_{-3.7}$	$11.05^{+0.03}_{-0.03}$	$10.73^{+0.07}_{-0.06}$
813055	149.881760	1.910661	0.7613	$-48.5^{+0.7}_{-0.7}$	$51.4^{+8.2}_{-7.2}$	3.4	50^{+24}_{-24}	82^{+9}_{-8}	$0.6^{+0.3}_{-0.3}$	$9.68^{+0.05}_{-0.05}$	$10.13^{+0.10}_{-0.09}$
824746	150.120987	2.208277	0.8467	$+33.7^{+0.7}_{-0.9}$	$73.6^{+3.8}_{-3.5}$	8.6	126^{+16}_{-16}	38^{+12}_{-5}	$3.3^{+1.1}_{-0.6}$	$9.84^{+0.04}_{-0.04}$	$10.58^{+0.10}_{-0.09}$
824408	150.196198	2.267904	0.7496	$+22.1^{+0.9}_{-0.8}$	$68.7^{+4.2}_{-3.9}$	5.3	117^{+7}_{-7}	44^{+12}_{-6}	$2.7^{+0.7}_{-0.4}$	$9.73^{+0.04}_{-0.04}$	$10.34^{+0.07}_{-0.05}$
831493	150.145020	2.336934	0.9360	$-40.7^{+0.5}_{-0.5}$	$61.3^{+2.4}_{-2.3}$	12.3	252^{+18}_{-17}	44^{+9}_{-5}	$5.8^{+1.3}_{-0.8}$	$10.59^{+0.04}_{-0.03}$	$11.29^{+0.06}_{-0.06}$
832277	150.009109	2.371844	1.0299	$-23.1^{+1.4}_{-1.5}$	$50.4^{+5.0}_{-4.6}$	7.4	159^{+12}_{-11}	24^{+24}_{-13}	$6.7^{+6.9}_{-3.8}$	$10.46^{+0.04}_{-0.04}$	$10.66^{+0.07}_{-0.06}$
832708	149.920853	2.306864	0.9272	$+26.5^{+0.6}_{-0.6}$	$61.3^{+4.3}_{-3.9}$	6.2	122^{+25}_{-25}	57^{+8}_{-5}	$2.1^{+0.5}_{-0.5}$	$10.28^{+0.04}_{-0.04}$	$10.50^{+0.13}_{-0.13}$
825250	150.024475	2.190769	0.7587	$+36.9^{+1.0}_{-1.0}$	$54.2^{+4.0}_{-3.7}$	7.9	225^{+14}_{-13}	36^{+15}_{-7}	$6.2^{+2.6}_{-1.3}$	$10.38^{+0.05}_{-0.05}$	$11.00^{+0.05}_{-0.05}$
825269	150.021332	2.178634	0.7954	$+34.6^{+0.7}_{-0.7}$	$57.2^{+3.7}_{-3.5}$	7.6	157^{+15}_{-15}	32^{+16}_{-8}	$4.8^{+2.5}_{-1.2}$	$9.79^{+0.05}_{-0.04}$	$10.68^{+0.08}_{-0.08}$
823909	150.304321	2.269336	0.9256	$-37.7^{+0.9}_{-0.9}$	$49.8^{+7.4}_{-6.7}$	4.8	242^{+29}_{-27}	40^{+11}_{-7}	$6.0^{+1.8}_{-1.2}$	$10.22^{+0.08}_{-0.05}$	$10.84^{+0.10}_{-0.09}$
824079	150.259933	2.292139	0.9871	$+4.2^{+0.4}_{-0.3}$	$71.4^{+3.8}_{-3.5}$	5.8	106^{+8}_{-8}	68^{+6}_{-4}	$1.6^{+0.2}_{-0.2}$	$10.10^{+0.04}_{-0.05}$	$10.46^{+0.05}_{-0.04}$
831094	150.228714	2.316025	0.8972	$-15.7^{+0.2}_{-0.2}$	$66.6^{+3.7}_{-3.4}$	5.6	138^{+10}_{-10}	73^{+4}_{-2}	$1.9^{+0.2}_{-0.1}$	$10.21^{+0.03}_{-0.04}$	$10.60^{+0.04}_{-0.04}$
826042	149.868927	2.130142	1.1774	$+21.2^{+0.3}_{-0.3}$	$79.0^{+5.0}_{-4.4}$	4.0	30^{+6}_{-6}	83^{+5}_{-4}	$0.4^{+0.1}_{-0.1}$	$9.75^{+0.03}_{-0.03}$	$10.16^{+0.05}_{-0.04}$
826065	149.864700	2.209825	0.8941	$-14.6^{+1.2}_{-1.6}$	$56.0^{+5.1}_{-4.7}$	6.7	104^{+19}_{-19}	57^{+9}_{-6}	$1.8^{+0.4}_{-0.4}$	$9.90^{+0.04}_{-0.04}$	$10.45^{+0.11}_{-0.10}$
826091	149.857941	2.137394	0.8937	$-31.0^{+1.0}_{-1.1}$	$57.9^{+3.8}_{-3.6}$	10.3	152^{+12}_{-12}	51^{+9}_{-6}	$3.0^{+0.6}_{-0.4}$	$10.03^{+0.05}_{-0.07}$	$10.84^{+0.06}_{-0.06}$
833167	149.836288	2.301956	0.9711	$+47.7^{+0.4}_{-0.4}$	$72.7^{+3.7}_{-3.4}$	5.8	8^{+6}_{-6}	59^{+6}_{-3}	$0.1^{+0.1}_{-0.1}$	$9.75^{+0.08}_{-0.05}$	$10.01^{+0.09}_{-0.04}$
833707	149.731277	2.329328	0.7841	$+44.9^{+0.5}_{-0.5}$	$63.2^{+3.0}_{-2.8}$	8.4	187^{+14}_{-14}	54^{+10}_{-7}	$3.5^{+0.7}_{-0.5}$	$10.21^{+0.03}_{-0.04}$	$10.90^{+0.06}_{-0.06}$
827090	149.659027	2.224841	0.9205	$+1.0^{+0.6}_{-0.6}$	$65.5^{+2.9}_{-2.7}$	11.1	136^{+21}_{-21}	42^{+10}_{-5}	$3.3^{+0.9}_{-0.6}$	$9.88^{+0.04}_{-0.05}$	$10.76^{+0.11}_{-0.11}$
830321	150.383362	2.371992	0.8500	$-7.1^{+1.0}_{-1.0}$	$60.8^{+10.4}_{-8.6}$	1.8	70^{+23}_{-23}	78^{+6}_{-4}	$0.9^{+0.3}_{-0.3}$	$9.17^{+0.03}_{-0.04}$	$9.88^{+0.09}_{-0.08}$
830414	150.369095	2.394953	0.9234	$+20.8^{+2.5}_{-2.0}$	$43.9^{+9.2}_{-8.2}$	4.4	45^{+32}_{-32}	74^{+12}_{-11}	$0.6^{+0.4}_{-0.4}$	$10.70^{+0.03}_{-0.04}$	$10.15^{+0.15}_{-0.14}$
837931	150.287567	2.477325	0.9018	$+0.7^{+0.5}_{-0.6}$	$66.0^{+8.3}_{-7.1}$	2.3	40^{+16}_{-16}	57^{+10}_{-8}	$0.7^{+0.3}_{-0.3}$	$9.90^{+0.03}_{-0.03}$	$9.67^{+0.14}_{-0.11}$
837433	150.378189	2.530785	0.7963	$-22.9^{+0.4}_{-0.5}$	$70.3^{+2.3}_{-2.2}$	12.0	192^{+4}_{-4}	27^{+28}_{-15}	$7.2^{+7.5}_{-4.1}$	$10.21^{+0.05}_{-0.05}$	$11.03^{+0.04}_{-0.03}$
837491	150.367355	2.520236	0.9940	$+11.9^{+0.5}_{-0.6}$	$68.3^{+2.9}_{-2.8}$	8.2	106^{+6}_{-6}	57^{+6}_{-3}	$1.8^{+0.2}_{-0.2}$	$9.80^{+0.04}_{-0.04}$	$10.54^{+0.05}_{-0.04}$
837613	150.341934	2.568233	0.8182	$-20.8^{+0.3}_{-0.3}$	$79.4^{+2.8}_{-2.6}$	7.7	105^{+7}_{-7}	37^{+14}_{-9}	$2.9^{+1.1}_{-0.7}$	$10.37^{+0.05}_{-0.05}$	$10.40^{+0.09}_{-0.06}$
831296	150.187332	2.414294	0.8517	$-12.7^{+0.4}_{-0.4}$	$61.4^{+4.7}_{-4.3}$	5.0	147^{+9}_{-9}	30^{+17}_{-9}	$4.8^{+2.7}_{-1.4}$	$9.97^{+0.06}_{-0.08}$	$10.44^{+0.06}_{-0.05}$
831848	150.082047	2.458241	0.9363	$-41.6^{+0.4}_{-0.4}$	$76.9^{+3.3}_{-3.1}$	6.4	162^{+43}_{-43}	105^{+10}_{-10}	$1.5^{+0.4}_{-0.4}$	$10.08^{+0.05}_{-0.04}$	$10.87^{+0.13}_{-0.13}$
832184	150.026810	2.403100	0.9468	$-31.7^{+1.9}_{-1.4}$	$45.3^{+6.4}_{-5.9}$	6.5	121^{+16}_{-15}	25^{+25}_{-14}	$4.9^{+5.0}_{-2.8}$	$10.00^{+0.15}_{-0.06}$	$10.39^{+0.13}_{-0.10}$
839193	150.058121	2.562992	0.8887	$-54.2^{+1.2}_{-1.5}$	$46.0^{+4.1}_{-3.8}$	10.4	125^{+10}_{-10}	25^{+27}_{-15}	$4.9^{+5.2}_{-2.9}$	$10.25^{+0.04}_{-0.04}$	$10.61^{+0.10}_{-0.07}$
839379	150.026962	2.589348	0.7469	$-44.3^{+1.5}_{-1.6}$	$52.0^{+5.3}_{-4.9}$	5.9	112^{+28}_{-28}	28^{+29}_{-16}	$4.1^{+4.4}_{-2.6}$	$9.59^{+0.04}_{-0.03}$	$10.29^{+0.22}_{-0.20}$
840437	149.842422	2.570137	0.9642	$+46.5^{+0.7}_{-0.8}$	$61.0^{+4.4}_{-4.0}$	6.2	121^{+40}_{-40}	60^{+7}_{-4}	$2.0^{+0.7}_{-0.7}$	$9.66^{+0.04}_{-0.04}$	$10.51^{+0.19}_{-0.19}$
701403	149.895996	2.410341	1.1694	$+51.2^{+2.8}_{-2.7}$	$54.1^{+5.5}_{-5.1}$	8.3	30^{+33}_{-33}	75^{+6}_{-4}	$0.4^{+0.4}_{-0.4}$	$9.57^{+0.05}_{-0.06}$	$10.39^{+0.09}_{-0.08}$
811012	150.331024	1.879742	0.8383	$+2.6^{+0.8}_{-0.9}$	$47.2^{+4.2}_{-4.0}$	7.0	10^{+10}_{-10}	46^{+9}_{-3}	$0.2^{+0.2}_{-0.2}$	$9.11^{+0.03}_{-0.04}$	$9.88^{+0.17}_{-0.06}$
811108	150.309006	1.916707	0.8963	$-55.8^{+0.9}_{-0.9}$	$54.1^{+3.6}_{-3.4}$	8.7	140^{+22}_{-22}	70^{+7}_{-5}	$2.0^{+0.4}_{-0.4}$	$10.31^{+0.03}_{-0.04}$	$10.79^{+0.10}_{-0.09}$
817640	150.296600	1.969438	0.9357	$+23.9^{+1.0}_{-1.1}$	$43.6^{+6.8}_{-6.2}$	5.4	211^{+32}_{-30}	34^{+13}_{-7}	$6.2^{+2.6}_{-1.6}$	$10.11^{+0.06}_{-0.08}$	$10.77^{+0.13}_{-0.12}$
817426	150.339340	2.100803	0.8667	$+9.9^{+0.6}_{-0.7}$	$63.4^{+3.5}_{-3.3}$	6.9	103^{+8}_{-8}	49^{+9}_{-4}	$2.1^{+0.4}_{-0.2}$	$9.97^{+0.05}_{-0.08}$	$10.40^{+0.07}_{-0.05}$
818113	150.192520	2.019528	1.0123	$+16.2^{+0.8}_{-0.9}$	$61.8^{+4.0}_{-3.7}$	6.5	137^{+9}_{-9}	41^{+9}_{-4}	$3.3^{+0.8}_{-0.4}$	$10.00^{+0.04}_{-0.03}$	$10.53^{+0.06}_{-0.05}$
811920	150.138062	1.881366	0.8342	$-9.5^{+1.0}_{-1.0}$	$65.4^{+3.1}_{-2.9}$	8.3	6^{+5}_{-5}	55^{+8}_{-3}	$0.1^{+0.1}_{-0.1}$	$9.76^{+0.04}_{-0.04}$	$10.09^{+0.12}_{-0.05}$
818734	150.074448	2.038712	0.8742	$+52.3^{+1.8}_{-1.5}$	$41.9^{+7.9}_{-7.2}$	5.1	8^{+9}_{-9}	49^{+8}_{-3}	$0.2^{+0.2}_{-0.2}$	$9.68^{+0.05}_{-0.04}$	$9.80^{+0.14}_{-0.06}$
813128	149.862106	1.936515	0.7887	$-13.7^{+0.8}_{-0.6}$	$61.9^{+2.9}_{-2.8}$	9.6	126^{+6}_{-6}	37^{+14}_{-7}	$3.5^{+1.3}_{-0.7}$	$9.97^{+0.04}_{-0.04}$	$10.62^{+0.06}_{-0.04}$
830282	150.388718	2.309891	0.7432	$-39.6^{+0.4}_{-0.6}$	$62.8^{+4.6}_{-4.2}$	4.9	152^{+15}_{-15}	29^{+15}_{-12}	$5.2^{+2.7}_{-2.2}$	$9.80^{+0.04}_{-0.04}$	$10.46^{+0.09}_{-0.08}$
831655	150.112289	2.387432	0.7573	$+22.0^{+0.3}_{-0.3}$	$74.1^{+2.2}_{-2.1}$	9.4	189^{+8}_{-8}	45^{+8}_{-6}	$4.2^{+0.8}_{-0.6}$	$10.28^{+0.04}_{-0.03}$	$10.94^{+0.04}_{-0.04}$
813411	149.793304	1.927607	0.7684	$-48.9^{+1.3}_{-1.2}$	$59.0^{+4.7}_{-4.3}$	7.0	20^{+9}_{-9}	31^{+10}_{-5}	$0.6^{+0.4}_{-0.3}$	$9.60^{+0.04}_{-0.04}$	$9.61^{+0.24}_{-0.13}$

Table E.2. [OII] measurements.

ID	$R_{[OII]}$	$EW([O\,II])$ Å	$E_s(B-V)_{SED}$	$\log(SFR_{SED}/M_\odot\,yr^{-1})$	$\log(SFR_{[OII],corr}/M_\odot\,yr^{-1})$
(1)	(2)	(3)	(4)	(5)	(6)
701002	0.51 ± 0.11	-17.57 ± 2.70	0.4	$1.15^{+0.08}_{-0.08}$	1.36 ± 0.13
701403	0.64 ± 0.06	-33.92 ± 1.70	0.2	$1.57^{+0.08}_{-0.08}$	1.33 ± 0.11
811012	0.72 ± 0.02	-93.06 ± 0.59	0.2	$1.35^{+0.07}_{-0.07}$	1.56 ± 0.11
811108	0.90 ± 0.09	-20.45 ± 0.99	0.3	$1.25^{+0.07}_{-0.07}$	1.37 ± 0.11
811224	0.49 ± 0.12	-8.16 ± 1.12	0.5	$1.65^{+0.07}_{-0.07}$	1.61 ± 0.12
811233	4.84 ± 7.38	-5.84 ± 0.75	0.5	$1.46^{+0.08}_{-0.08}$	1.22 ± 0.12
811727	0.16 ± 0.06	-11.11 ± 0.80	0.4	$1.98^{+0.38}_{-0.09}$	1.62 ± 0.11
811920	0.76 ± 0.04	-35.48 ± 0.82	0.3	$1.53^{+0.08}_{-0.09}$	1.49 ± 0.11
812913	0.82 ± 0.28	-10.75 ± 0.93	0.1	$-0.08^{+0.09}_{-0.13}$	0.16 ± 0.12
813055	0.56 ± 0.07	-17.57 ± 0.88	0.3	$0.83^{+0.09}_{-0.11}$	0.84 ± 0.11
813128	0.54 ± 0.05	-14.56 ± 1.08	0.3	$1.03^{+0.08}_{-0.07}$	0.99 ± 0.11
817262	1.04 ± 0.11	-25.19 ± 1.61	0.3	$1.31^{+0.35}_{-0.13}$	1.32 ± 0.11
817416	0.78 ± 0.07	-60.95 ± 3.35	0.2	$1.25^{+0.07}_{-0.07}$	1.48 ± 0.11
817426	0.70 ± 0.04	-36.01 ± 0.78	0.2	$1.02^{+0.21}_{-0.10}$	1.17 ± 0.11
817640	0.63 ± 0.04	-23.93 ± 0.65	0.3	$1.35^{+0.13}_{-0.24}$	1.33 ± 0.11
818113	0.61 ± 0.03	-30.20 ± 0.60	0.3	$1.55^{+0.07}_{-0.07}$	1.55 ± 0.11
818198	0.84 ± 0.06	-25.12 ± 0.64	0.3	$1.21^{+0.09}_{-0.22}$	1.30 ± 0.11
818734	0.68 ± 0.03	-26.35 ± 0.87	0.2	$1.02^{+0.10}_{-0.12}$	0.93 ± 0.11
818959	0.72 ± 0.12	-10.11 ± 1.53	0.3	$1.18^{+0.11}_{-0.44}$	0.73 ± 0.13
819479	0.63 ± 0.05	-18.54 ± 0.61	0.1	$0.47^{+0.23}_{-0.10}$	0.08 ± 0.11
819641	0.99 ± 0.17	-5.12 ± 1.17	0.5	$1.54^{+0.07}_{-0.07}$	1.26 ± 0.15
819765	0.43 ± 0.07	-18.44 ± 1.06	0.5	$1.32^{+0.09}_{-0.22}$	1.57 ± 0.11
823045	0.63 ± 0.13	-12.66 ± 0.88	0.3	$0.95^{+0.07}_{-0.07}$	0.95 ± 0.11
823323	0.83 ± 0.56	-8.94 ± 0.89	0.6	$2.20^{+0.09}_{-0.10}$	1.84 ± 0.12
823909	0.80 ± 0.08	-10.67 ± 0.58	0.5	$1.83^{+0.08}_{-0.08}$	1.49 ± 0.11
824079	0.81 ± 0.05	-37.16 ± 1.07	0.3	$1.15^{+0.07}_{-0.07}$	1.54 ± 0.11
824317	0.62 ± 0.08	-24.97 ± 2.40	0.3	$1.34^{+0.08}_{-0.08}$	1.36 ± 0.12
824384	0.61 ± 0.11	-27.33 ± 2.32	0.3	$0.85^{+0.07}_{-0.07}$	1.33 ± 0.12
824408	0.76 ± 0.06	-15.16 ± 0.72	0.3	$0.75^{+0.07}_{-0.07}$	0.73 ± 0.11
824508	0.62 ± 0.06	-15.33 ± 1.11	0.3	$1.20^{+0.09}_{-0.08}$	1.29 ± 0.11
824658	1.04 ± 0.09	-14.12 ± 0.96	0.5	$1.45^{+0.07}_{-0.07}$	1.66 ± 0.11
824675	0.57 ± 0.08	-14.05 ± 0.69	0.2	$0.78^{+0.10}_{-0.09}$	0.72 ± 0.11
824746	0.72 ± 0.04	-36.28 ± 1.27	0.3	$1.22^{+0.08}_{-0.07}$	1.27 ± 0.11
824791	0.74 ± 0.73	-12.09 ± 1.31	0.3	$0.75^{+0.08}_{-0.07}$	0.70 ± 0.12
824847	1.42 ± 0.34	-15.26 ± 1.81	0.5	$1.70^{+0.29}_{-0.10}$	1.58 ± 0.12
825250	0.64 ± 0.06	-13.09 ± 0.84	0.3	$0.99^{+0.08}_{-0.09}$	1.00 ± 0.11
825269	0.76 ± 0.04	-31.02 ± 1.37	0.3	$1.14^{+0.07}_{-0.08}$	1.40 ± 0.11
825474	0.95 ± 0.11	-11.41 ± 0.65	0.2	$0.97^{+0.08}_{-0.08}$	0.82 ± 0.11
826042	0.67 ± 0.05	-79.53 ± 3.06	0.3	$1.95^{+0.07}_{-0.07}$	2.12 ± 0.11
826065	0.61 ± 0.07	-35.86 ± 2.57	0.2	$0.66^{+0.07}_{-0.07}$	0.93 ± 0.11

Notes. (1) Source HR-COSMOS identification number; (2) [OII]λ3729/[OII]λ3726 ratio; (3) [OII] rest-frame equivalent width; (4) color excess of the stellar continuum coming from the SED fitting process; (5) log(*SFR*) derived from the SED fitting process (Sect. 2.4); (6) log(*SFR*) derived from the [OII] EW corrected for internal extinction (Sect. C).

Table E.2. continued.

ID	$R_{[OII]}$	$EW([O\,II])$ Å	$E_s(B-V)_{SED}$	$\log(SFR_{SED}/M_\odot\,yr^{-1})$	$\log(SFR_{[OII],corr}/M_\odot\,yr^{-1})$
(1)	(2)	(3)	(4)	(5)	(6)
826091	0.64 ± 0.08	-24.15 ± 1.44	0.2	$0.80^{+0.27}_{-0.10}$	0.84 ± 0.11
826948	0.68 ± 0.08	-31.07 ± 1.40	0.4	$1.94^{+0.07}_{-0.07}$	1.94 ± 0.11
827050	0.93 ± 0.16	-59.94 ± 2.73	0.4	$1.15^{+0.07}_{-0.07}$	2.21 ± 0.11
827090	0.72 ± 0.03	-25.75 ± 0.95	0.2	$1.14^{+0.08}_{-0.07}$	1.10 ± 0.11
827096	0.87 ± 0.08	-22.07 ± 1.19	0.4	$1.34^{+0.08}_{-0.07}$	1.58 ± 0.11
829955	0.54 ± 0.16	-6.37 ± 0.99	0.4	$2.06^{+0.07}_{-0.08}$	1.27 ± 0.13
830321	0.83 ± 0.05	-51.77 ± 1.79	0.1	$0.85^{+0.07}_{-0.07}$	0.75 ± 0.11
830414	0.45 ± 0.06	-25.83 ± 2.15	0.1	$0.15^{+0.07}_{-0.07}$	0.50 ± 0.11
831094	0.70 ± 0.03	-54.53 ± 0.63	0.3	$1.45^{+0.07}_{-0.07}$	1.96 ± 0.11
831223	1.11 ± 0.41	-5.05 ± 3.84	0.7	$1.18^{+0.10}_{-0.20}$	1.11 ± 0.35
831229	0.72 ± 0.18	-10.36 ± 1.95	0.4	$0.55^{+0.14}_{-0.32}$	0.63 ± 0.14
831256	0.58 ± 0.06	-18.12 ± 0.81	0.6	$1.65^{+0.24}_{-0.15}$	1.76 ± 0.11
831296	0.42 ± 0.03	-23.76 ± 0.98	0.2	$0.92^{+0.44}_{-0.11}$	0.87 ± 0.11
831493	0.73 ± 0.05	-19.80 ± 1.20	0.4	$1.45^{+0.07}_{-0.07}$	1.72 ± 0.11
831534	1.53 ± 0.50	-8.53 ± 1.10	0.1	$-0.15^{+0.07}_{-0.07}$	0.17 ± 0.12
831675	1.51 ± 0.26	-6.62 ± 0.60	0.5	$1.64^{+0.07}_{-0.07}$	1.53 ± 0.12
831848	0.99 ± 0.20	-25.87 ± 1.78	0.4	$1.75^{+0.07}_{-0.07}$	1.71 ± 0.11
832184	1.30 ± 0.36	-16.48 ± 0.65	0.4	$1.66^{+0.12}_{-0.52}$	1.45 ± 0.11
832277	0.69 ± 0.07	-24.77 ± 1.27	0.4	$1.43^{+0.08}_{-0.08}$	1.73 ± 0.11
832385	0.32 ± 0.08	-30.10 ± 2.76	0.5	$1.58^{+0.29}_{-0.14}$	1.73 ± 0.12
832708	0.70 ± 0.05	-26.13 ± 1.03	0.2	$1.15^{+0.07}_{-0.07}$	1.24 ± 0.11
833167	0.80 ± 0.04	-36.15 ± 1.27	0.2	$1.07^{+0.11}_{-0.16}$	1.20 ± 0.11
833209	1.20 ± 0.08	-31.71 ± 1.64	0.2	$1.43^{+0.08}_{-0.07}$	1.29 ± 0.11
833707	0.89 ± 0.10	-10.61 ± 1.04	0.4	$1.14^{+0.08}_{-0.08}$	1.15 ± 0.12
833862	0.52 ± 0.11	-23.83 ± 1.32	0.6	$1.42^{+0.08}_{-0.07}$	1.69 ± 0.11
834100	1.13 ± 0.09	-44.41 ± 3.31	0.2	$0.96^{+0.07}_{-0.07}$	1.02 ± 0.11
837355	0.71 ± 0.04	-47.27 ± 3.80	0.1	$0.55^{+0.07}_{-0.07}$	0.61 ± 0.11
837433	0.71 ± 0.13	-9.18 ± 0.74	0.3	$0.95^{+0.07}_{-0.07}$	0.80 ± 0.11
837491	0.80 ± 0.04	-30.12 ± 1.08	0.2	$1.08^{+0.08}_{-0.09}$	1.09 ± 0.11
837613	0.50 ± 0.08	-20.38 ± 1.45	0.4	$1.15^{+0.08}_{-0.08}$	1.26 ± 0.11
837931	0.63 ± 0.05	-19.21 ± 0.76	0.0	$0.05^{+0.07}_{-0.07}$	-0.17 ± 0.11
838455	0.22 ± 0.06	-6.93 ± 1.64	0.4	$1.47^{+0.08}_{-0.08}$	1.05 ± 0.15
839193	1.09 ± 0.30	-15.99 ± 1.38	0.3	$1.25^{+0.07}_{-0.07}$	1.22 ± 0.12
839379	0.61 ± 0.05	-12.90 ± 0.54	0.2	$0.65^{+0.07}_{-0.07}$	0.37 ± 0.11
840112	0.26 ± 0.11	-4.55 ± 0.64	0.2	$0.62^{+0.25}_{-0.11}$	0.17 ± 0.12
840266	0.91 ± 0.06	-28.39 ± 1.12	0.3	$1.31^{+0.48}_{-0.11}$	1.48 ± 0.11
840390	0.47 ± 0.05	-15.25 ± 0.79	0.4	$1.25^{+0.07}_{-0.07}$	1.34 ± 0.11
840437	0.62 ± 0.04	-30.57 ± 1.08	0.2	$1.05^{+0.07}_{-0.07}$	1.09 ± 0.11
1 254 477	0.57 ± 0.06	-22.02 ± 1.17	0.4	$1.42^{+0.09}_{-0.23}$	1.63 ± 0.11